Centrality and transverse momentum dependence of D^0-meson production at mid-rapidity in Au+Au collisions at $\sqrt{s_{\mathrm{NN}}} = 200\,\mathrm{GeV}$

J. Adam[12], L. Adamczyk[2], J. R. Adams[34], J. K. Adkins[25], G. Agakishiev[23], M. M. Aggarwal[36], Z. Ahammed[56], I. Alekseev[3,30], D. M. Anderson[50], R. Aoyama[53], A. Aparin[23], D. Arkhipkin[5], E. C. Aschenauer[5], M. U. Ashraf[52], F. Atetalla[24], A. Attri[36], G. S. Averichev[23], V. Bairathi[31], K. Barish[9], A. J. Bassill[9], A. Behera[48], R. Bellwied[19], A. Bhasin[22], A. K. Bhati[36], J. Bielcik[13], J. Bielcikova[33], L. C. Bland[5], I. G. Bordyuzhin[3], J. D. Brandenburg[5], A. V. Brandin[30], D. Brown[27], J. Bryslawskyj[9], I. Bunzarov[23], J. Butterworth[41], H. Caines[59], M. Calderón de la Barca Sánchez[7], D. Cebra[7], I. Chakaberia[24,45], P. Chaloupka[13], B. K. Chan[8], F-H. Chang[32], Z. Chang[5], N. Chankova-Bunzarova[23], A. Chatterjee[56], S. Chattopadhyay[56], J. H. Chen[46], X. Chen[44], J. Cheng[52], M. Cherney[12], W. Christie[5], G. Contin[26], H. J. Crawford[6], M. Csanad[15], S. Das[10], T. G. Dedovich[23], I. M. Deppner[18], A. A. Derevschikov[38], L. Didenko[5], C. Dilks[37], X. Dong[26], J. L. Drachenberg[1], J. C. Dunlop[5], T. Edmonds[39], L. G. Efimov[23], N. Elsey[58], J. Engelage[6], G. Eppley[41], R. Esha[8], S. Esumi[53], O. Evdokimov[11], J. Ewigleben[27], O. Eyser[5], R. Fatemi[25], S. Fazio[5], P. Federic[33], J. Fedorisin[23], P. Filip[23], E. Finch[47], Y. Fisyak[5], C. E. Flores[7], L. Fulek[2], C. A. Gagliardi[50], T. Galatyuk[14], F. Geurts[41], A. Gibson[55], L. Greiner[26], D. Grosnick[55], D. S. Gunarathne[49], Y. Guo[24], A. Gupta[22], W. Guryn[5], A. I. Hamad[24], A. Hamed[50], A. Harlenderova[13], J. W. Harris[59], L. He[39], S. Heppelmann[7], S. Heppelmann[37], N. Herrmann[18], A. Hirsch[39], L. Holub[13], Y. Hong[26], S. Horvat[59], B. Huang[11], H. Z. Huang[8], S. L. Huang[48], T. Huang[32], X. Huang[52], T. J. Humanic[34], P. Huo[48], G. Igo[8], W. W. Jacobs[20], A. Jentsch[51], J. Jia[5,48], K. Jiang[44], S. Jowzaee[58], X. Ju[44], E. G. Judd[6], S. Kabana[24], S. Kagamaster[27], D. Kalinkin[20], K. Kang[52], D. Kapukchyan[9], K. Kauder[5], H. W. Ke[5], D. Keane[24], A. Kechechyan[23], M. Kelsey[26], D. P. Kikoła [57], C. Kim[9], T. A. Kinghorn[7], I. Kisel[16], A. Kisiel[57], M. Kocan[13], L. Kochenda[30], L. K. Kosarzewski[13], A. F. Kraishan[49], L. Kramarik[13], L. Krauth[9], P. Kravtsov[30], K. Krueger[4], N. Kulathunga Mudiyanselage[19], L. Kumar[36], R. Kunnawalkam Elayavalli[58], J. Kvapil[13], J. H. Kwasizur[20], R. Lacey[48], J. M. Landgraf[5], J. Lauret[5], A. Lebedev[5], R. Lednicky[23], J. H. Lee[5], C. Li[44], W. Li[46], W. Li[41], X. Li[44], Y. Li[52], Y. Liang[24], R. Licenik[13], J. Lidrych[13], T. Lin[50], A. Lipiec[57], M. A. Lisa[34], F. Liu[10], H. Liu[20], P. Liu[48], P. Liu[46], X. Liu[34], Y. Liu[50], Z. Liu[44], T. Ljubicic[5], W. J. Llope[58], M. Lomnitz[26], R. S. Longacre[5], S. Luo[11], X. Luo[10], G. L. Ma[46], L. Ma[17], R. Ma[5], Y. G. Ma[46], N. Magdy[11], R. Majka[59], D. Mallick[31], S. Margetis[24], C. Markert[51], H. S. Matis[26], O. Matonoha[13], J. A. Mazer[42], K. Meehan[7], J. C. Mei[45], N. G. Minaev[38], S. Mioduszewski[50], D. Mishra[31], B. Mohanty[31], M. M. Mondal[21], I. Mooney[58], Z. Moravcova[13], D. A. Morozov[38], M. Mustafa[26], Md. Nasim[8], K. Nayak[10], J. M. Nelson[6], D. B. Nemes[59], M. Nie[46], G. Nigmatkulov[30], T. Niida[58], L. V. Nogach[38], T. Nonaka[10], G. Odyniec[26], A. Ogawa[5], K. Oh[40], S. Oh[59], V. A. Okorokov[30], D. Olvitt Jr.[49], B. S. Page[5], R. Pak[5], Y. Panebratsev[23], B. Pawlik[35], H. Pei[10], C. Perkins[6], R. L. Pinter[15], J. Pluta[57], J. Porter[26], M. Posik[49], N. K. Pruthi[36], M. Przybycien[2], J. Putschke[58], A. Quintero[49], H. Qiu[26], S. K. Radhakrishnan[26], R. L. Ray[51], R. Reed[27], H. G. Ritter[26], J. B. Roberts[41], O. V. Rogachevskiy[23], J. L. Romero[7], L. Ruan[5], J. Rusnak[33], O. Rusnakova[13], N. R. Sahoo[50], P. K. Sahu[21], S. Salur[42], J. Sandweiss[59], J. Schambach[51], A. M. Schmah[26], W. B. Schmidke[5], N. Schmitz[28], B. R. Schweid[48], F. Seck[14], J. Seger[12], M. Sergeeva[8], R. Seto[9], P. Seyboth[28], N. Shah[46], E. Shahaliev[23], P. V. Shanmuganathan[27], M. Shao[44], F. Shen[45], W. Q. Shen[46], S. S. Shi[10], Q. Y. Shou[46], E. P. Sichtermann[26], S. Siejka[57], R. Sikora[2], M. Simko[33], JSingh[36], S. Singha[24], D. Smirnov[5], N. Smirnov[59], W. Solyst[20], P. Sorensen[5], H. M. Spinka[4], B. Srivastava[39], T. D. S. Stanislaus[55], D. J. Stewart[59], M. Strikhanov[30], B. Stringfellow[39], A. A. P. Suaide[43], T. Sugiura[53], M. Sumbera[33], B. Summa[37], X. M. Sun[10], Y. Sun[44], B. Surrow[49], D. N. Svirida[3], M. Szelezniak[26], P. Szymanski[57], A. H. Tang[5], Z. Tang[44], A. Taranenko[30], T. Tarnowsky[29], J. H. Thomas[26], A. R. Timmins[19], T. Todoroki[5], M. Tokarev[23], C. A. Tomkiel[27], S. Trentalange[8], R. E. Tribble[50], P. Tribedy[5], S. K. Tripathy[21], O. D. Tsai[8], B. Tu[10], T. Ullrich[5], D. G. Underwood[4], I. Upsal[5,45], G. Van Buren[5], J. Vanek[33], A. N. Vasiliev[38], I. Vassiliev[16], F. Videbæk[5], S. Vokal[23], S. A. Voloshin[58], A. Vossen[20], F. Wang[39], G. Wang[8], P. Wang[44], Y. Wang[10], Y. Wang[52], J. C. Webb[5], L. Wen[8], G. D. Westfall[29], H. Wieman[26], S. W. Wissink[20], R. Witt[54], Y. Wu[24], Z. G. Xiao[52], G. Xie[11], W. Xie[39], N. Xu[26], Q. H. Xu[45], Y. F. Xu[46], Z. Xu[5], C. Yang[45], Q. Yang[45], S. Yang[5], Y. Yang[32], Z. Ye[41], Z. Ye[11], L. Yi[45], K. Yip[5], I. -K. Yoo[40], H. Zbroszczyk[57], W. Zha[44], D. Zhang[10], J. Zhang[48], L. Zhang[10], S. Zhang[44], S. Zhang[46], X. P. Zhang[52], Y. Zhang[44], Z. Zhang[46], J. Zhao[39], C. Zhong[46], C. Zhou[46], X. Zhu[52], Z. Zhu[45], M. K. Zurek[26], M. Zyzak[16]

[1]*Abilene Christian University, Abilene, Texas 79699*
[2]*AGH University of Science and Technology, FPACS, Cracow 30-059, Poland*
[3]*Alikhanov Institute for Theoretical and Experimental Physics, Moscow 117218, Russia*
[4]*Argonne National Laboratory, Argonne, Illinois 60439*
[5]*Brookhaven National Laboratory, Upton, New York 11973*

[6]University of California, Berkeley, California 94720
[7]University of California, Davis, California 95616
[8]University of California, Los Angeles, California 90095
[9]University of California, Riverside, California 92521
[10]Central China Normal University, Wuhan, Hubei 430079
[11]University of Illinois at Chicago, Chicago, Illinois 60607
[12]Creighton University, Omaha, Nebraska 68178
[13]Czech Technical University in Prague, FNSPE, Prague 115 19, Czech Republic
[14]Technische Universität Darmstadt, Darmstadt 64289, Germany
[15]Eötvös Loránd University, Budapest, Hungary H-1117
[16]Frankfurt Institute for Advanced Studies FIAS, Frankfurt 60438, Germany
[17]Fudan University, Shanghai, 200433
[18]University of Heidelberg, Heidelberg 69120, Germany
[19]University of Houston, Houston, Texas 77204
[20]Indiana University, Bloomington, Indiana 47408
[21]Institute of Physics, Bhubaneswar 751005, India
[22]University of Jammu, Jammu 180001, India
[23]Joint Institute for Nuclear Research, Dubna 141 980, Russia
[24]Kent State University, Kent, Ohio 44242
[25]University of Kentucky, Lexington, Kentucky 40506-0055
[26]Lawrence Berkeley National Laboratory, Berkeley, California 94720
[27]Lehigh University, Bethlehem, Pennsylvania 18015
[28]Max-Planck-Institut für Physik, Munich 80805, Germany
[29]Michigan State University, East Lansing, Michigan 48824
[30]National Research Nuclear University MEPhI, Moscow 115409, Russia
[31]National Institute of Science Education and Research, HBNI, Jatni 752050, India
[32]National Cheng Kung University, Tainan 70101
[33]Nuclear Physics Institute of the CAS, Rez 250 68, Czech Republic
[34]Ohio State University, Columbus, Ohio 43210
[35]Institute of Nuclear Physics PAN, Cracow 31-342, Poland
[36]Panjab University, Chandigarh 160014, India
[37]Pennsylvania State University, University Park, Pennsylvania 16802
[38]Institute of High Energy Physics, Protvino 142281, Russia
[39]Purdue University, West Lafayette, Indiana 47907
[40]Pusan National University, Pusan 46241, Korea
[41]Rice University, Houston, Texas 77251
[42]Rutgers University, Piscataway, New Jersey 08854
[43]Universidade de São Paulo, São Paulo, Brazil 05314-970
[44]University of Science and Technology of China, Hefei, Anhui 230026
[45]Shandong University, Qingdao, Shandong 266237
[46]Shanghai Institute of Applied Physics, Chinese Academy of Sciences, Shanghai 201800
[47]Southern Connecticut State University, New Haven, Connecticut 06515
[48]State University of New York, Stony Brook, New York 11794
[49]Temple University, Philadelphia, Pennsylvania 19122
[50]Texas A&M University, College Station, Texas 77843
[51]University of Texas, Austin, Texas 78712
[52]Tsinghua University, Beijing 100084
[53]University of Tsukuba, Tsukuba, Ibaraki 305-8571, Japan
[54]United States Naval Academy, Annapolis, Maryland 21402
[55]Valparaiso University, Valparaiso, Indiana 46383
[56]Variable Energy Cyclotron Centre, Kolkata 700064, India
[57]Warsaw University of Technology, Warsaw 00-661, Poland
[58]Wayne State University, Detroit, Michigan 48201 and
[59]Yale University, New Haven, Connecticut 06520

(STAR Collaboration)

(Dated: December 7, 2018)

We report a new measurement of D^0-meson production at mid-rapidity ($|y|$ <1) in Au+Au collisions at $\sqrt{s_{\rm NN}} = 200$ GeV utilizing the Heavy Flavor Tracker, a high resolution silicon detector at the STAR experiment. Invariant yields of D^0-mesons in the transverse momentum (p_T) $<\sim 9\,{\rm GeV}/c$ are reported in various centrality bins (0–10%, 10–20%, 20–40%, 40–60% and 60–80%). Blast-Wave thermal models are used to fit the D^0-meson p_T spectra to study D^0 hadron kinetic freeze-out properties. The average radial flow velocity extracted from the fit is considerably smaller than that of light hadrons (π, K, p), but comparable to that of hadrons containing multiple strange quarks

(ϕ, Ξ^-), indicating that D^0 mesons kinetically decouple from the system earlier than light hadrons. The calculated D^0 nuclear modification factors re-affirm that charm quarks suffer large amount of energy loss in the medium, similar to those of light quarks for $p_T > 4\,\mathrm{GeV}/c$ in central 0–10% Au+Au collisions. At low p_T, the nuclear modification factor shows a characteristic structure consistent with the expectation from model predictions that charm quarks gain sizable collective motion during the medium evolution. The new improved measurements are expected to offer further constraints to model calculations and help gain new insights to the hot and dense medium created in these collisions.

I. INTRODUCTION

The heavy ion program at the Relativistic Heavy Ion Collider (RHIC) and Large Hadron Collider (LHC) focuses on the study of strong interactions and Quantum Chromodynamics (QCD) at high temperature and density. Over the last few papers, experimental results from RHIC and LHC using light flavor probes have demonstrated that a strongly-coupled Quark-Gluon Plasma (sQGP) is created in these heavy-ion collisions. The most significant evidence comes from the strong collective flow and the large high transverse momentum (p_T) suppression in central collisions for various observed hadrons including multi-strange-quark hadrons ϕ and Ω [1–5].

Heavy quarks (c,b) are created predominantly through initial hard scatterings due to their large masses [6, 7]. The modification to their production in transverse momentum due to energy loss and radial flow and in azimuth due to anisotropic flows is sensitive to heavy quark dynamics in the partonic sQGP phase [8]. Recent measurements of high-p_T D-meson production at RHIC and LHC show a strong suppression in the central heavy-ion collisions [9–12]. The suppression is often characterized by the nuclear modification factor R_{AA}, defined as

$$R_{\mathrm{AA}}(p_T) = \frac{1}{\langle T_{\mathrm{AA}} \rangle} \frac{dN_{\mathrm{AA}}/dp_T}{d\sigma_{pp}/dp_T}. \tag{1}$$

where dN_{AA}/dp_T and $d\sigma_{pp}/dp_T$ are particle production yield and cross section in A+A and p+p collisions, respectively. The nuclear thickness function $T_{\mathrm{AA}} = \langle N_{\mathrm{bin}} \rangle / \sigma_{pp}^{\mathrm{inel}}$ is often calculated using a Monte-Carlo Glauber model, where $\langle N_{\mathrm{bin}} \rangle$ is the average number of binary collisions and $\sigma_{pp}^{\mathrm{inel}}$ is the total inelastic p+p cross section. The D-meson R_{AA} is similar to that of light hadrons at $p_T > 4\,\mathrm{GeV}/c$, suggesting significant energy loss for charm quarks inside the sQGP medium. The measured D-meson anisotropic flow shows that D-mesons also exhibit significant elliptic and triangular flow at RHIC and LHC [13–16]. The flow magnitude when scaled with the transverse kinetic energy is similar to that of light and strange flavor hadrons. This indicates that charm quarks may behave like they reached thermal equilibrium in these collisions at RHIC and LHC.

In this article, we report measurements of the centrality dependence of D^0-meson transverse momentum spectra at mid-rapidity ($|y| < 1$) in Au+Au collisions at $\sqrt{s_{\mathrm{NN}}} = 200\,\mathrm{GeV}$. The measurements are conducted at the Solenoidal Tracker At RHIC (STAR) experiment utilizing the high resolution silicon detector (the Heavy Flavor Tracker, HFT) [17]. The paper is organized in the following order: In Sec. II, we describe the detector setup and dataset used in this analysis. In Sec. III, we present the topological reconstruction of D^0 mesons in the Au+Au collision data, followed by Sec. IV and Sec. V for details on efficiency corrections and systematic uncertainties. We present our measurement results and physics discussions in Sec. VI. Finally, we end the paper with a summary in Sec. VII .

II. EXPERIMENTAL SETUP AND DATASET

The dataset used in this analysis consists of Au+Au collision events at $\sqrt{s_{\mathrm{NN}}} = 200\,\mathrm{GeV}$ collected in the 2014 year run. The main detectors used in this analysis are the Time Projection Chamber (TPC), the HFT, the Time of Flight (TOF) detector and the Vertex Position Detector (VPD).

A. Tracking and Particle Identification Subsystems

Precision tracking for this analysis is achieved with TPC and HFT detectors and particle identification for stable hadrons are performed with a combination of the ionization energy loss (dE/dx) measurement with the TPC and the time-of-flight (tof) measurement with TOF detector. The event start time is provided by the VPD. Both TPC and TOF detectors have full azimuthal coverage with a pseudo-rapidity range of $|\eta| < 1$ [18, 19]. The TPC and TOF subsystems have been extensively used in many prior STAR analyses, including D-meson measurements [4, 12, 20]. The HFT detector provides measured space points with high precision that are used to extend track trajectories and offer high-pointing resolution to the vicinity of the event vertex.

B. Trigger and Dataset

The minimum bias trigger used in this analysis is defined as a coincidence between the east and west VPD detectors located at $4.4 < |\eta| < 4.9$ [21]. Each VPD detector is an assembly of nineteen small detectors, each consisting of a Pb converter followed by a fast, plastic scintillator read out by a photo multiplier tube. To efficiently sample the collision events in the center of the HFT acceptance, an online cut of collision vertex along the beam line (calculated via the time difference between east and west VPD detectors) $|V_z^{\mathrm{VPD}}| < 6\,\mathrm{cm}$ is applied. The decrease in the coincidence probability in VPD degrades the online VPD vertex resolution in peripheral low multiplicity events. These inefficiencies are corrected in the offline analysis with a method to be discussed in the next section.

Events used in this analysis are selected with the offline reconstructed collision vertex (namely Primary Vertex - PV, V_z^{TPC}) within 6 cm of the TPC and HFT centers along the beam direction to ensure uniform and large acceptance. The maximum total drift time of ionization electrons inside the TPC is about $40\,\mu\mathrm{s}$ while the hadronic Au+Au collision rate is typically around 40 kHz when this dataset was recorded. There is a finite chance that more than one event is recorded in the TPC readout event frame. The VPD is a fast detector which can separate events from different bunch crossings (one bunch cross at RHIC is 106 ns). In order to suppress the chance of selecting the wrong vertex from collisions happening in bunch crossings different from that of the trigger, the difference between the event vertex z coordinate V_z^{TPC} and the V_z^{VPD} is required to be less than 3 cm. Approximately 9×10^8 minimum bias triggered events with 0–80% centrality pass the selection criteria and are used in this analysis.

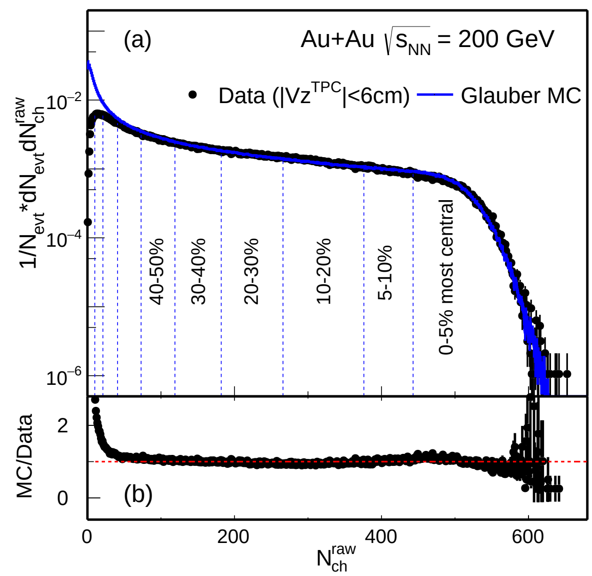

FIG. 1. (a) Uncorrected charged particle multiplicity $N_{\mathrm{ch}}^{\mathrm{raw}}$ distribution measured within $|\eta| < 0.5$ and $|V_z^{\mathrm{TPC}}| < 6\,\mathrm{cm}$. The solid curve depicts the multiplicity distribution from a MC Glauber simulation fit to the experimental data. (b) Ratio between MC simulation and real data.

C. Centrality Selection and Trigger Inefficiency

The centrality is selected using the measured charged global track multiplicity $N_{\mathrm{ch}}^{\mathrm{raw}}$ at mid-rapidity within $|\eta| < 0.5$ and corrected for the online VPD triggering inefficiency using a Monte Carlo (MC) Glauber simulation. 0–X% centrality is defined as the 0–X% most central in terms of total hadronic cross section determined by the impact parameter between two colliding nuclei. In this analysis, the dependence of $N_{\mathrm{ch}}^{\mathrm{raw}}$ on the collision vertex position and the beam luminosity has been taken into account. The measured track multiplicity distribution from Au+Au 200 GeV from RHIC run 2014, corrected for the vertex and luminosity dependence, is shown in Fig. 1. The measured distribution is fit to the MC Glauber calculation in the high multiplicity region. One can observe that the fitted MC Glauber calculation matches the real data well for $N_{\mathrm{ch}}^{\mathrm{raw}} > 100$, while the discrepancy in the low multiplicity region shows the VPD trigger inefficiency. Figure 1 panel (b) shows the ratio between MC and data. Centrality is defined according to the MC Glauber model distribution shown in panel (a). Events in the low-multiplicity region are weighted with the ratio shown in panel (b) in all the following analysis as a correction for the inefficiency in trigger.

Table I lists the extracted values of average number of binary collisions (N_{bin}), number of participants (N_{part}) and trigger inefficiency correction factors ($\varepsilon_{\mathrm{trg}}$) and their uncertainties in various centrality bins. The $\varepsilon_{\mathrm{trg}}$ correction factor is applied event-by-event in the analysis to obtain physics measurements when combining centrality bins.

D. Heavy Flavor Tracker

The HFT [17] is a high resolution silicon detector system that aims for topological reconstruction of secondary vertices from heavy flavor hadron decays. It consists of three silicon subsystems: the Silicon Strip Detector (SSD), the Intermediate Silicon Tracker (IST), and two layers of the PiXeL (PXL) detector. Table II lists the key characteristic parameters of each subsystem. The SSD detector was still under commissioning when the dataset was recorded, and therefore is not used in the offline data production and this analysis. The PXL detector uses the new Monolithic Active Pixel Sensors (MAPS) technology [17]. This is the first application of this technology in a collider experiment. It is specifically designed to measure heavy flavor hadron decays in the high multiplicity heavy-ion collision environment.

In the offline reconstruction, tracks are reconstructed in the TPC first and then extended to the HFT detector to find the best fit to the measured high resolution spatial points. Kalman filter algorithm that considers various detector material effects is used in the track extension. Considering the background hits level in the PXL detector due to pileup hadronic and electromagnetic collisions, tracks are required to have at least one hit in each layer of PXL and IST sub-detectors. Figure 2 shows the track pointing resolution to the primary vertex

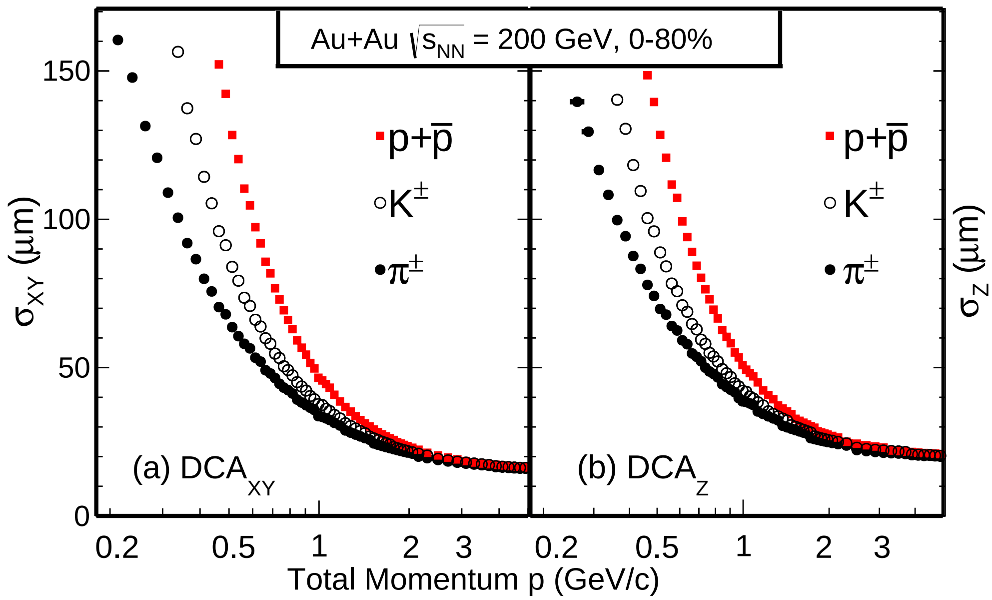

FIG. 2. Identified particle ($\pi^{\pm}$, $K^{\pm}$, and $p+\bar{p}$) pointing resolution in the transverse (a) and longitudinal (b) planes as a function of particle total momentum in Au+Au 0–80% collisions.

TABLE I. Estimated values of average number of binary collisions ($N_{\rm bin}$), number of participants ($N_{\rm part}$) and trigger correction factors ($\varepsilon_{\rm trg}$, uncertainties negligible) for various centrality bins obtained from the MC Glauber model fit to the measured multiplicity distributions.

Centrality	$\langle N_{\rm bin}\rangle$	$\langle N_{\rm part}\rangle$	$\varepsilon_{\rm trg}$
0–10 %	938.8 ± 26.3	319.4 ± 3.4	1.0
10–20 %	579.9 ± 28.8	227.6 ± 7.9	1.0
20–40 %	288.3 ± 30.4	137.6 ± 10.4	1.0
40–60 %	91.3 ± 21.0	60.5 ± 10.1	0.92
60–80 %	21.3 ± 8.9	20.4 ± 6.6	0.65

in the transverse plane ($\sigma_{\rm XY}$) in panel (a) and along the longitudinal direction ($\sigma_{\rm Z}$) in panel (b) as a function of total momentum (p) for identified particles in 0–80% centrality Au+Au collisions. The design goal for the HFT detector was to have a pointing resolution better than 55 μm for 750 MeV charged kaon particles. Figure 2 demonstrates that the HFT detector system meets the design requirements. This performance enables precision measurement of D-meson production in high multiplicity heavy-ion collisions.

III. D^0-MESON RECONSTRUCTION

D^0 and $\overline{D}^0$ mesons are reconstructed via the hadronic decay channel $D^0 \rightarrow K^- + \pi^+$ and its charge conjugate channel with a branching ratio ($B.R.$) of 3.89%. In what follows, we imply $(D^0+\overline{D}^0)/2$ when using the term D^0 unless otherwise specified. D^0 mesons decay with a proper decay length of $c\tau \sim 123$ μm after they are produced in Au+Au collisions. We utilize the high-pointing resolution capability enabled by the HFT detector to topologically reconstruct the D^0 decay vertices that are separated from the collision vertices, which drastically reduces the combinatorial background ($\sim$five orders of magnitude) and improves the measurement precision.

Charged pion and kaon tracks are reconstructed with the TPC and the HFT. Tracks are required to have at least 20 measured TPC points out of maximum 45 to ensure with good momentum resolution. To enable high pointing precision, both daughter tracks are required to have at least one measured hit in each layer of PXL and IST as described above. Particle identification is achieved via a combination of the ionization energy loss measurement in the TPC and the tof measurement in the TOF. The resolution-normalized dE/dx deviation from the expected values is defined as:

$$n\sigma_X = \frac{1}{R}\ln\frac{\langle dE/dx\rangle_{mea.}}{\langle dE/dx\rangle_X}, \tag{2}$$

TABLE II. Several key characteristic parameters for each subsystem of the STAR HFT detector.

Subsystem	Radius (cm)	Length (cm)	Thickness at $\eta = 0$ (X_0)	Pitch Size (μm^2)
PXL inner layer	2.8	20	0.52% (0.39%†)	20.7×20.7
PXL outer layer	8.0	20	0.52%	20.7×20.7
IST	14.0	50	1.0%	600×6000
SSD††	22.0	106	1.0%	95×40000

† - PXL inner detector material is reduced to 0.39%X_0 in 2015/2016 runs.
†† - SSD is not included in this analysis.

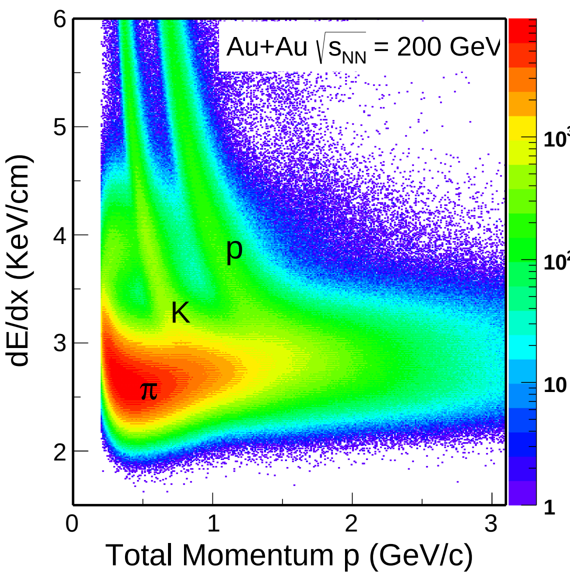

FIG. 3. TPC dE/dx vs. particle momentum.

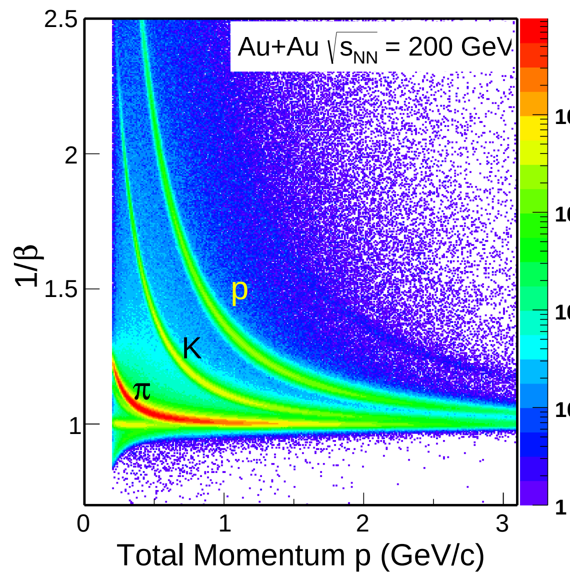

FIG. 4. TOF $1/\beta$ vs. particle momentum.

where $\langle dE/dx\rangle_{mea.}$ and $\langle dE/dx\rangle_X$ represent measured and expected values with a hypothesis of particle X, and R is the dE/dx resolution (typically $\sim$8% [18]). The $n\sigma_X$ should be close to a standard Gaussian distribution for each corresponding particle species (mean = 0, σ = 1) with good dE/dx calibration. Pion (kaon) candidates are selected by a requirement of the measured dE/dx to be within three (two) standard deviations ($|n\sigma_X|$) from the expected value. When tracks have matched hits in the TOF detector, an additional requirement on the measured inverse particle velocity ($1/\beta$) to be within three standard deviations from the expected value ($|\Delta 1/\beta|$) is applied for either daughter track. Figures. 3 and 4 show examples of the particle identification capability from TPC and TOF. Tracks within the kinematic acceptance $p_T > 0.6$ GeV/c and $|\eta| < 1$ are used to combine and make pairs. Table III lists the TPC and TOF selection cuts for daughter kaon and pion tracks used for D^0 reconstruction.

With a pair of two daughter tracks, pion and kaon, D^0 decay vertex is reconstructed as the middle point on the distance of the closest approach between the two daughter trajectories. One of the dominant background source is the random combination of fake pairs directly from the collision point. With the selection of the following topological variables, the background level can be greatly reduced.

TABLE III. TPC and TOF selection cuts for K and π tracks.

Variable		$K^{\mp}$	$\pi^{\pm}$
p_T (GeV/c)	$>$	0.6	0.6
$\lvert\eta\rvert$	$<$	1.0	1.0
nHitsFit (TPC)	$>$	20	20
$\lvert n\sigma_X\rvert$	$<$	2.0	3.0
$\lvert\Delta 1/\beta\rvert$ (if TOF matched)	$<$	0.03	0.03

- Decay Length: the distance between the reconstructed decay vertex and the Primary Vertex (PV, $V_z^{\rm TPC}$).
- Distance of Closest Approach (DCA) between the two daughter tracks (DCA$_{12}$).
- DCA between the reconstructed D^0 and the PV (DCA$_{D^0}$).
- DCA between the pion and the PV (DCA$_{\pi}$).
- DCA between the kaon and the PV (DCA$_{K}$).

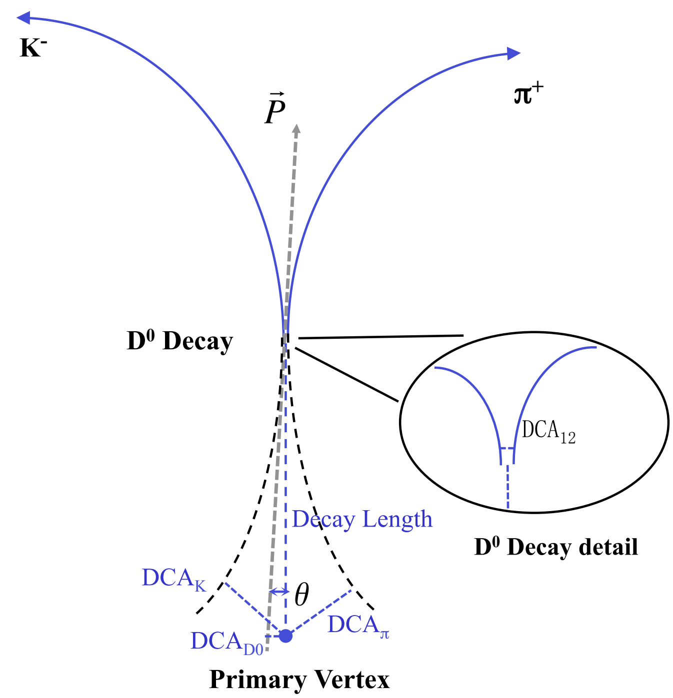

FIG. 5. A cartoon picture for $D^0 \to K^- + \pi^+$ decay and definition of topological variables used in the reconstruction.

- Angle between D^0 momentum and the direction of the decay vertex with respect to the PV (θ).

The schematic in Fig. 5 also shows the topological variables used in the analysis, where $\vec{P}$ represents the D^0 momentum. The Decay Length and angle θ follow the formula: $\mathrm{DCA}_{\mathrm{D^0}}$ = Decay Length $\times \sin(\theta)$. The cuts on the topological variables for this analysis are optimized using a Toolkit for Multivariate Data Analysis (TMVA) package [22] developed by CERN in order to obtain the greatest signal significance. The Rectangular Cut Optimization method from the TMVA package is chosen in this analysis, similar as in our previous publication [16]. The optimization is conducted for different D^0 p_T bins and different centrality bins. Table IV lists a set of topological cuts for 0–10% central Au+Au collisions.

Figure 6 shows the invariant mass distributions of $K\pi$ pairs in the p_T region of 0–10 GeV/c and 0–8 GeV/c for three different centrality bins, 0–80% minimum bias collisions, 0–10% most central and 60–80% peripheral collisions, respectively. The reason of choosing a different p_T range for the 60–80% centrality bin is because no signal is observed beyond the current statistics. The combinatorial background is estimated with the same-event (SE) like-sign (LS) pairs (blue histograms) and the mixed-event (ME) unlike-sign (US) (grey histograms) technique in which K and π from different events of similar characteristics (V_Z, centrality, event plane angle) are paired. The mixed-event spectra are normalized to the like-sign distributions in the mass range of 1.7–2.1 GeV/c^2. After the subtraction of the mixed-event unlike-sign combinatorial background from the same-event unlike-sign pairs (black open circles), the remainder distributions are shown as red solid circles in the each panel. Compared to the previous D^0 measurement [12], the D^0 signal significance is largely improved by a factor of ~ 15 using the same amount of event statistics.

Figures 7 and 8 show the invariant mass distributions in the same centrality bins as Fig. 6 but for different p_T ranges: $0 < p_T < 0.5\,\mathrm{GeV}/c$ in Fig. 7 and $6 < p_T < 8\,\mathrm{GeV}/c$ in Fig. 8.

After the combinatorial background is subtracted, the residual $K\pi$ invariant mass distributions are then fit to a Gaussian plus linear function. The linear function is used to represent some remaining correlated background from either partial reconstruction of charm mesons or jet fragments. The D^0 raw yields are extracted from the Gaussian function fit results while different choices of fit ranges, background functional forms, histogram counting vs. fitting methods etc. have been used to estimated systematic uncertainties on the raw yield extraction. See Sec. V for details.

IV. EFFICIENCIES AND CORRECTIONS

The reconstructed D^0 raw yields are calculated in each centrality, p_T bin, and within the rapidity window $|y| < 1$. The fully corrected D^0 production invariant yields are

TABLE IV. Topological cuts used for D^0 reconstruction in 0–10% most central collisions for separate p_T intervals.

$0 - -10\%$ | p_T (GeV/c)		(0,0.5)	(0.5,1)	(1,2)	(2,3)	(3,5)	(5,8)	(8,10)
Decay Length (μm)	>	100	199	227	232	236	255	255
DCA_{12} (μm)	<	71	64	70	63	82	80	80
$\mathrm{DCA}_{\mathrm{D}^0}$ (μm)	<	62	55	40	40	40	44	44
DCA_{π} (μm)	>	133	105	93	97	67	55	55
$\mathrm{DCA}_{\mathrm{K}}$ (μm)	>	138	109	82	94	76	54	54
$\cos(\theta)$	>	0.95	0.95	0.95	0.95	0.95	0.95	0.95

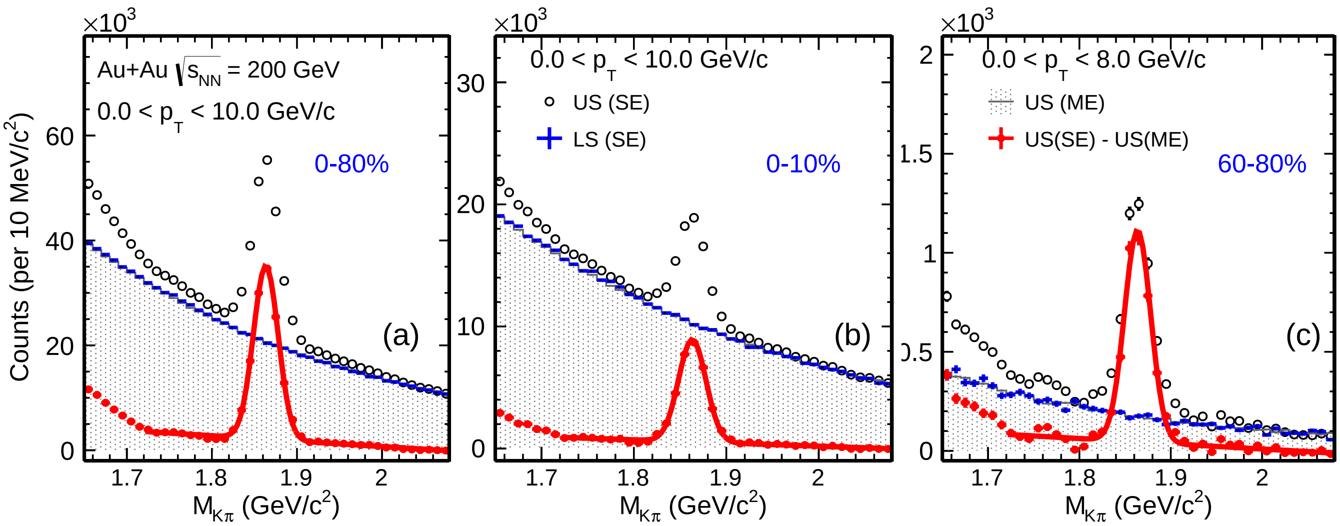

FIG. 6. Invariant mass $M_{K\pi}$ distributions in $0 < p_T < 10\,\mathrm{GeV}/c$ from centrality bins 0–80% (a), 0–10% (b) and $0 < p_T < 8\,\mathrm{GeV}/c$ for 60–80% (c), respectively. Black open circles represent the same-event (SE) unlike-sign (US) distributions. Blue and grey shaded histograms represent the SE like-sign (LS) and mixed-event (ME) US distributions that are used to estimate the combinatorial background. The red solid circles depict the US (SE) distributions with the combinatorial background subtracted using the US (ME) distributions.

calculated using the following formula:

$$\frac{d^2N}{2\pi p_T dp_T dy} = \frac{1}{\mathrm{B.R.}} \times \frac{N^{\mathrm{raw}}}{N_{\mathrm{evt}} 2\pi p_T \Delta p_T \Delta y} \times \frac{1}{\varepsilon_{\mathrm{trg}} \times \varepsilon_{\mathrm{TPC}} \times \varepsilon_{\mathrm{HFT}} \times \varepsilon_{\mathrm{PID}} \times \varepsilon_{\mathrm{vtx}}}, \quad (3)$$

where B.R. is the $D^0 \to K^-\pi^+$ decay branching ratio, $(3.89\pm0.04)\%$ [23], N^{raw} is the reconstructed D^0 raw counts, N_{evt} is the total numbers of events used in this analysis, $\varepsilon_{\mathrm{trg}}$ is the centrality bias correction factor described in Sec. II B. The raw yields need to be corrected for the TPC acceptance and tracking efficiency - $\varepsilon_{\mathrm{TPC}}$, the HFT acceptance and tracking plus topological cut efficiency - $\varepsilon_{\mathrm{HFT}}$, the particle identification efficiency - $\varepsilon_{\mathrm{PID}}$, and the finite vertex resolution correction - $\varepsilon_{\mathrm{vtx}}$.

A. TPC Acceptance and Tracking Efficiency - $\varepsilon_{\mathrm{TPC}}$

The TPC acceptance and tracking efficiency is obtained using the standard STAR TPC embedding technique, in which a small amount of MC tracks (typically 5% of the total multiplicity of the real event) are processed through the full GEANT simulation [24], then mixed with the raw Data Acquisition (DAQ) data in real events and reconstructed through the same reconstruction chain as the real data production. The TPC efficiency is then calculated as the ratio of the reconstructed MC tracks with the same offline analysis cuts for geometric acceptance and other TPC requirements to the input MC tracks.

Figure 9 shows the TPC acceptance and tracking efficiency $\varepsilon_{\mathrm{TPC}}$ for D^0 mesons within $|y| < 1$ in various centrality classes in this analysis. The efficiencies include the TPC and analysis acceptance cuts $p_T > 0.6\,\mathrm{GeV}/c$ and $|\eta| < 1$ as well as the TPC tracking efficiency for both pion and kaon daughters. The lower efficiency observed in central collisions is due to the increased multiplicity resulting higher detector occupancy which leads to reduced tracking efficiency in these collisions.

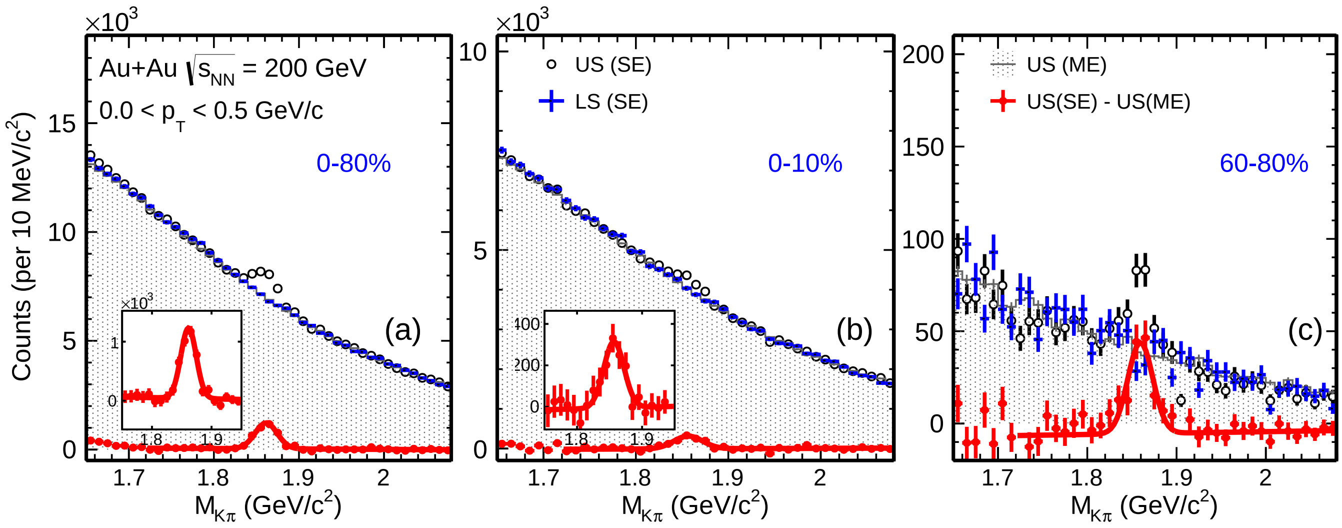

FIG. 7. Invariant mass $M_{K\pi}$ distributions in $0 < p_T < 0.5\,\mathrm{GeV}/c$ from centrality bins 0–80% (a), 0–10% (b) and 60–80% (c), respectively. All histograms and markers use the same notation as in Fig. 6.

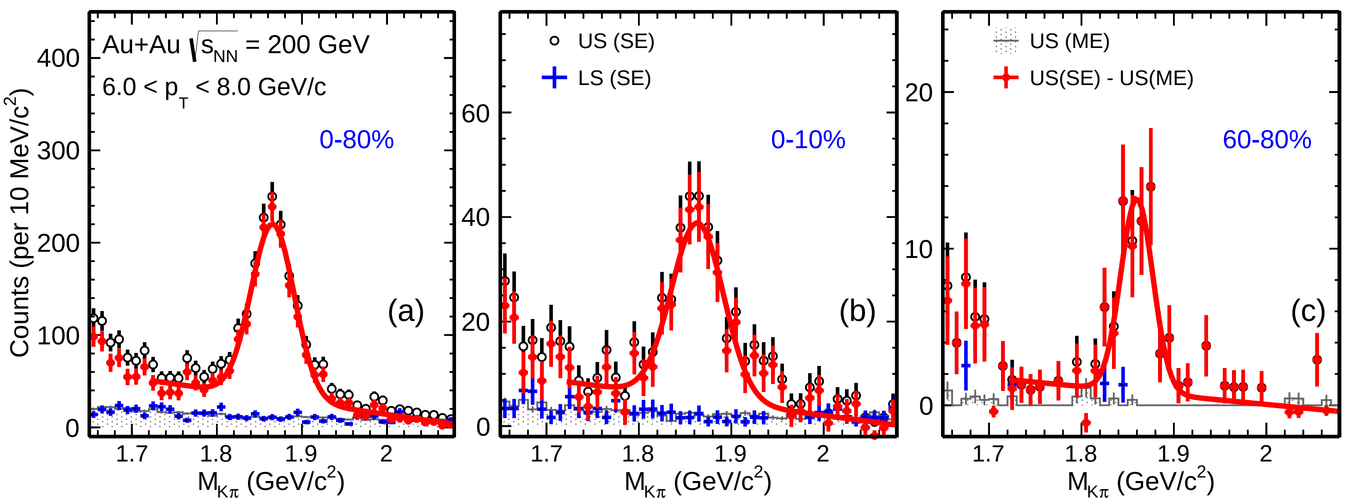

FIG. 8. Invariant mass $M_{K\pi}$ distributions in $6 < p_T < 8\,\mathrm{GeV}/c$ from centrality bins 0–80% (a), 0–10% (b) and 60–80% (c), respectively. All histograms and markers use the same notation as in Fig. 6.

B. HFT Acceptance, Tracking and Topological Cut Efficiency - $\varepsilon_{\mathrm{HFT}}$

1. *Data-driven Simulation*

In order to fully capture the real-time detector performance, the HFT-related efficiency is obtained using a data-driven simulation method in this analysis. The performance of inclusive HFT tracks is characterized by a TPC-to-HFT matching efficiency ($\varepsilon_{\mathrm{HFT}}^{\mathrm{match}}$) and the DCA distributions with respect to the primary vertex. The HFT matching efficiency $\varepsilon_{\mathrm{HFT}}^{\mathrm{match}}$ is defined as the fraction of reconstructed TPC tracks that satisfy the number of HFT hits requirement. In this analysis, the requirement is to have at least one hit in each PXL and IST layer. The $\varepsilon_{\mathrm{HFT}}^{\mathrm{match}}$ includes the HFT geometric acceptance and the tracking efficiency that associate HFT hits to the extended TPC tracks. It contains the true matches for which the reconstructed tracks pick up real physical hits induced by these charged tracks when passing through the HFT, as well as some random fake matches. The latter has a decreasing trend as a function of p_T as the track pointing resolution gets better at high p_T resulting in a smaller search window when associating HFT hits in the tracking algorithm. The DCA distributions are obtained for those tracks that satisfy the HFT hit requirement. These distributions obtained from real data are fed into a Monte Carlo decay generator for $D^0 \to K^-\pi^+$, followed by the same reconstruction of D^0 secondary vertex as in the real data analysis. The same topological cuts are

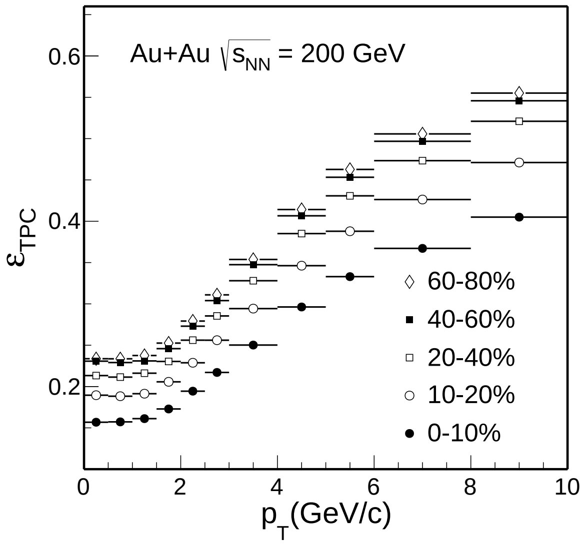

FIG. 9. D^0 TPC acceptance and tracking efficiencies from different centrality classes in Au+Au collisions at $\sqrt{s_{\rm NN}}$ = 200 GeV.

then applied and the HFT related efficiency for the D^0 reconstruction is calculated.

To best represent the real detector performance, we obtain the following distributions from real data in this Monte Carlo approach.

- Centrality-dependent $\mathrm{V_z}$ distributions.
- HFT matching efficiency $\varepsilon_{\rm HFT}^{\rm match}$, including the dependence on particle species, centrality, p_T, η, ϕ, and $\mathrm{V_z}$.
- $\mathrm{DCA_{XY}}$–$\mathrm{DCA_Z}$ 2-dimensional (2D) distributions including the dependence on particle species, centrality, p_T, η, and $\mathrm{V_z}$.

The $\mathrm{DCA_{XY}}$–$\mathrm{DCA_Z}$ 2D distributions are the key to represent not only the true matches, but also the fake matches when connecting the TPC tracks with HFT hits. The distributions are obtained in 2D to consider the correlation between the two quantities and this is necessary and essential to reproduce the 3D DCA position distributions observed in real data. The ϕ dependence of these distributions are integrated over due to computing resource limits. We have checked the ϕ dependence (by reducing other dependencies for the same reason) and it gives a consistent result compared to the ϕ-integrated one.

In total, there are 11 (ϕ) × 10 (η) × 6 ($\mathrm{V_z}$) × 9 (centrality) × 2 (particles) 1D histograms (36 p_T bins each) used for the HFT match efficiency distributions and 5 (η) × 4 ($\mathrm{V_z}$) × 9 (centrality) × 2 (particles) × 19 (p_T) 2D histograms (144 $\mathrm{DCA_{XY}}$ × 144 $\mathrm{DCA_Z}$ bins) for 2D DCA distributions. The number of bins chosen is optimized to balance the need of computing resources as well as the stability of the final efficiency. All dimensions have been checked so that further increase in the number of bins (in balance we need to reduce the number of bins in other dimensions) will not change the final obtained efficiency.

The procedure for this data-driven simulation package for efficiency calculation is as follows:

- Sample $\mathrm{V_z}$ distribution according to the distribution obtained from the real data.
- Generate D^0 at the event vertex position with desired p_T (Levy function shape fitted to D^0 spectra) and rapidity (flat) distributions.
- Propagate D^0 and simulate its decay to $K^-\pi^+$ daughters following the decay probability.
- Smear daughter track momentum according to the values obtained from embedding.
- Smear daughter track starting position according to the $\mathrm{DCA_{XY}}$–$\mathrm{DCA_Z}$ 2D distributions from the reconstructed data.
- Apply HFT matching efficiency according to that extracted from the reconstructed data.
- Do the topological reconstruction of D^0 decay vertices with the same cuts as applied in data analysis and calculate the reconstruction efficiency.

The distributions used as the input in this simulation tool can be obtained from the real data or the reconstructed data in MC simulation. The latter is used when we validate this approach using the MC GEANT simulation.

This approach assumes these distributions obtained from real data are good representations for tracks produced at or close to the primary vertices. The impact of the secondary particle contribution will be discussed in Sec. IV B 4. The approach also neglects the finite event vertex resolution contribution which will be discussed in Sec. IV C.

Lastly in this MC approach, we also fold in the TPC efficiency obtained from the MC embedding so the following presented efficiency will be the total efficiency of $\varepsilon_{\rm TPC} \times \varepsilon_{\rm HFT}$.

2. *Validation with GEANT Simulation*

In this subsection, we will demonstrate that the data-driven MC approach has been validated with the GEANT simulation plus the offline tracking reconstruction with realistic HFT detector performance to reproduce the real D^0 reconstruction efficiency. We should point out that in this validation procedure, what we are after is the efficiency difference between two calculation methods: one from the MC simulation directly, and the other one from the data-driven simulation package using the reconstructed MC simulation data as the input.

The GEANT simulation uses the HIJING [25] generator as its input with D^0 particles embedded to enrich the

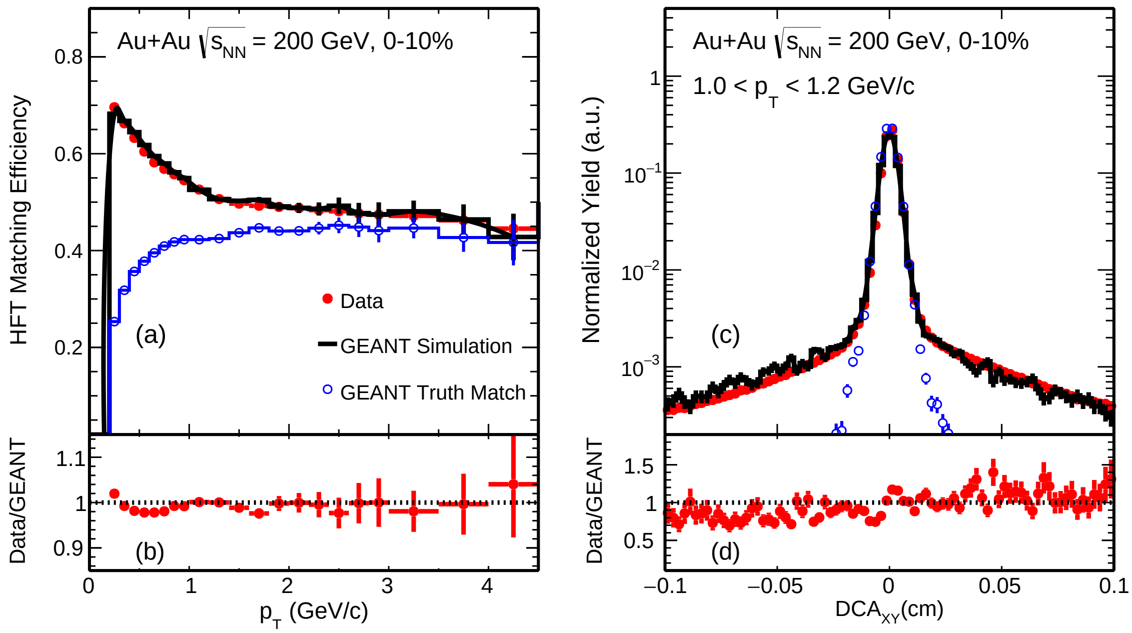

FIG. 10. HFT matching efficiency $\varepsilon_{\rm HFT}^{rmmatch}$ (a) and DCA$_{\rm XY}$ (c) distributions of inclusive charged pions from real data and MC simulation in 0–10% Au+Au collisions. The ratios between real data and GEANT simulation are shown in the bottom panels. The blue histogram depicts the true matches for which the reconstructed tracks pick up the correct MC hits in the HFT detector induced by the associated MC tracks in the GEANT simulation.

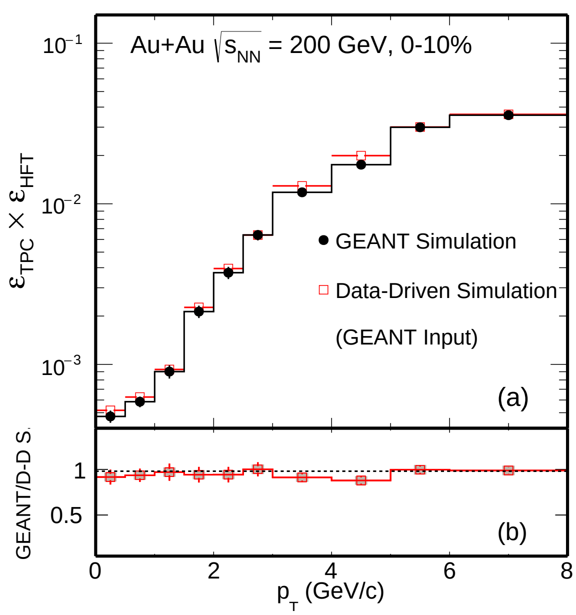

FIG. 11. D^0 reconstruction efficiency comparison between MC GEANT simulation (*black*) and data-driven fast simulation with reconstructed MC data as the input as the input (*red*) in central 0–10% Au+Au collisions.

signal statistics. The full HFT detector material including both active and inactive material have been included in the GEANT simulation as well as the offline track reconstruction. The pileup hits in the PXL detector due to finite electronic readout time have been added to realistically represent the HFT match efficiency and DCA distributions. Figure 10 shows an example of the HFT matching ratio and the 1-D projection of the DCA$_{\rm XY}$ distribution for single pions at $1.0 < p_T < 1.2\,{\rm GeV}/c$ and 0–10% central collisions. The overall agreements between the GEANT simulation and real data satisfy our need for this validation. The small deviation between real data and MC simulation in these distributions are not systematic uncertainties in our analyses since we are not calculating the absolute efficiency from this simulation sample directly.

The increase in the HFT matching efficiency at low p_T range is due to the increased fake matches (in contrast to true HFT matches) and the efficiency stays flat in the high p_T range. The matching efficiency includes the tracking efficiency when including the HFT hits as well as the HFT geometric acceptance. Therefore the ratio has a strong dependence on the event V$_{\rm Z}$ and the track η. The DCA distributions used in the package are 2-dimentional distributions, as DCA$_{\rm XY}$ and DCA$_{\rm Z}$ are strongly correlated.

With the tuned simulation setup, we use this sample to validate our data-driven simulation approach for D^0 efficiency calculation. We follow the same procedure as described in Sec. IV B 1 to obtain the HFT match efficiency as well as the 2D DCA$_{\rm XY}$-DCA$_{\rm Z}$ distributions for primary particles from the reconstructed data in this simulation sample. Then these distributions are fed into the data-driven simulation to calculate the D^0 reconstruction

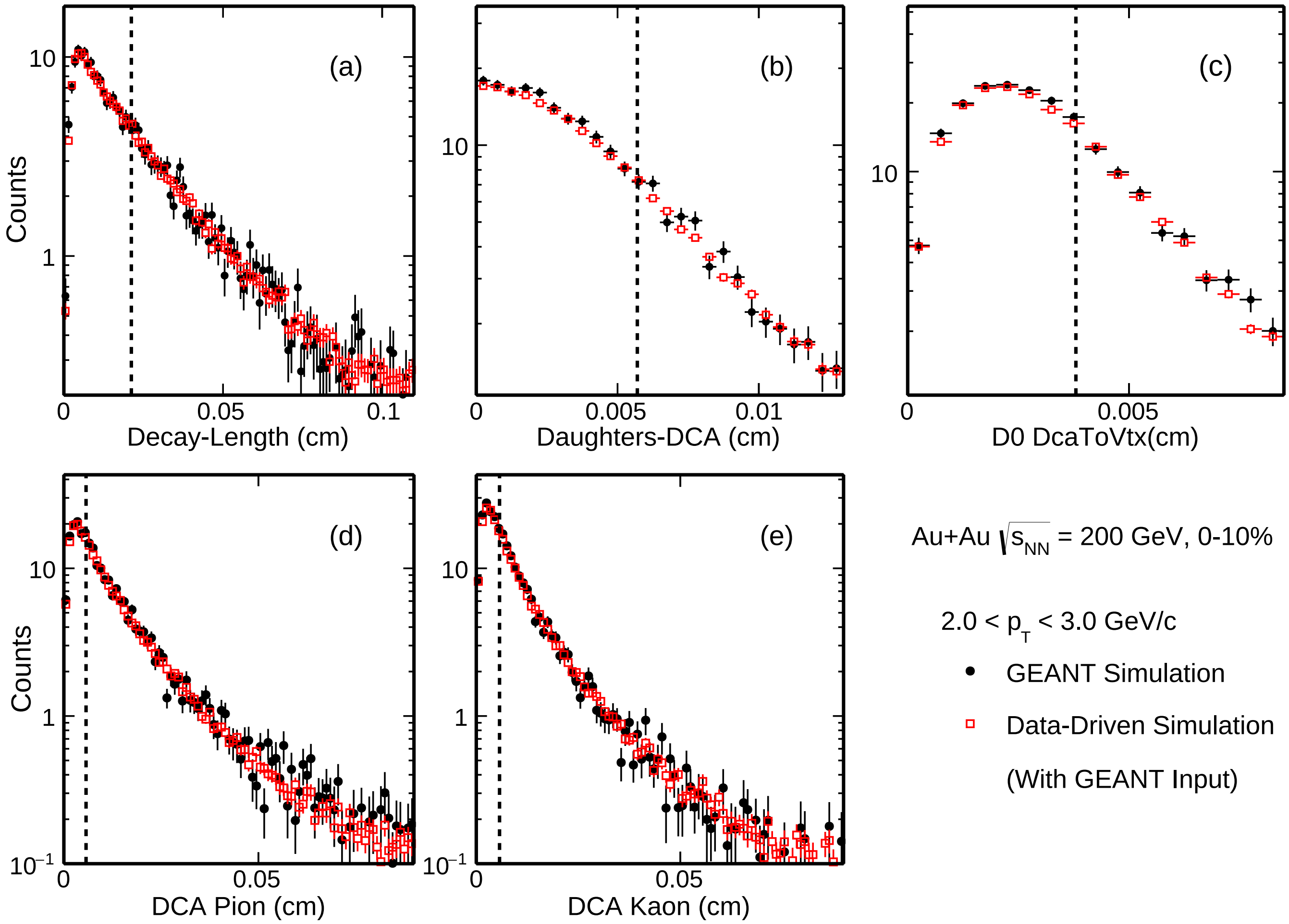

FIG. 12. Comparisons in topological variable distributions between MC GEANT simulation (*black*) and data-driven fast simulation with reconstructed MC data as the input (*red*) in 0–10% Au+Au collisions for D^0 mesons at $2 < p_T < 3\,\mathrm{GeV}/c$.

efficiency. This will be compared to the real D^0 reconstruction efficiency directly obtained from the GEANT simulation sample.

To validate the data-driven simulation tool, Fig. 12 shows the comparisons of several topological variables used in the D^0 reconstruction obtained from the GEANT simulation directly and from the data-driven simulation with the extract distributions from the GEANT simulation as the input in the most central (0–10%) centrality and in $2 < p_T < 3\,\mathrm{GeV}/c$. The topological variables shown here are D^0 decay length, DCA between two D^0 decay daughters, D^0 DCA with respect to the collision vertex, pion DCA and kaon DCA with respect to the collision vertex. As seen in this figure, the data-driven simulation tool reproduces all of these topological distributions quite well. The agreements for the other p_T ranges are also quite good.

Figure 11 shows the D^0 reconstruction efficiency $\varepsilon_{\mathrm{TPC}} \times \varepsilon_{\mathrm{HFT}}$ calculated with the following two methods in this GEANT simulation. The first method is the standard calculation by applying the tracking and topological cuts for reconstructed D^0 mesons in the simulation sample. In the second method, we employ the data-driven simulation method and take the reconstructed distributions from the simulation sample as the input and then calculate the D^0 reconstruction efficiency in the data-driven simulation framework. In panel (a) of Fig. 11, efficiencies from two calculation methods agree well in the whole p_T region in central 0–10% Au+Au collisions, and the ratio between the two is shown in panel (b). This demonstrates that the data-driven simulation framework can accurately reproduce the real D^0 reconstruction efficiency in central Au+Au collisions.

3. *Efficiency for real data*

We employ the validated data-driven simulation method for the real data analysis. Figure 13 shows comparisons of the same five topological variables between D^0 signals in real data and data-driven simulated distributions with real data as the input in central 0–10% col-

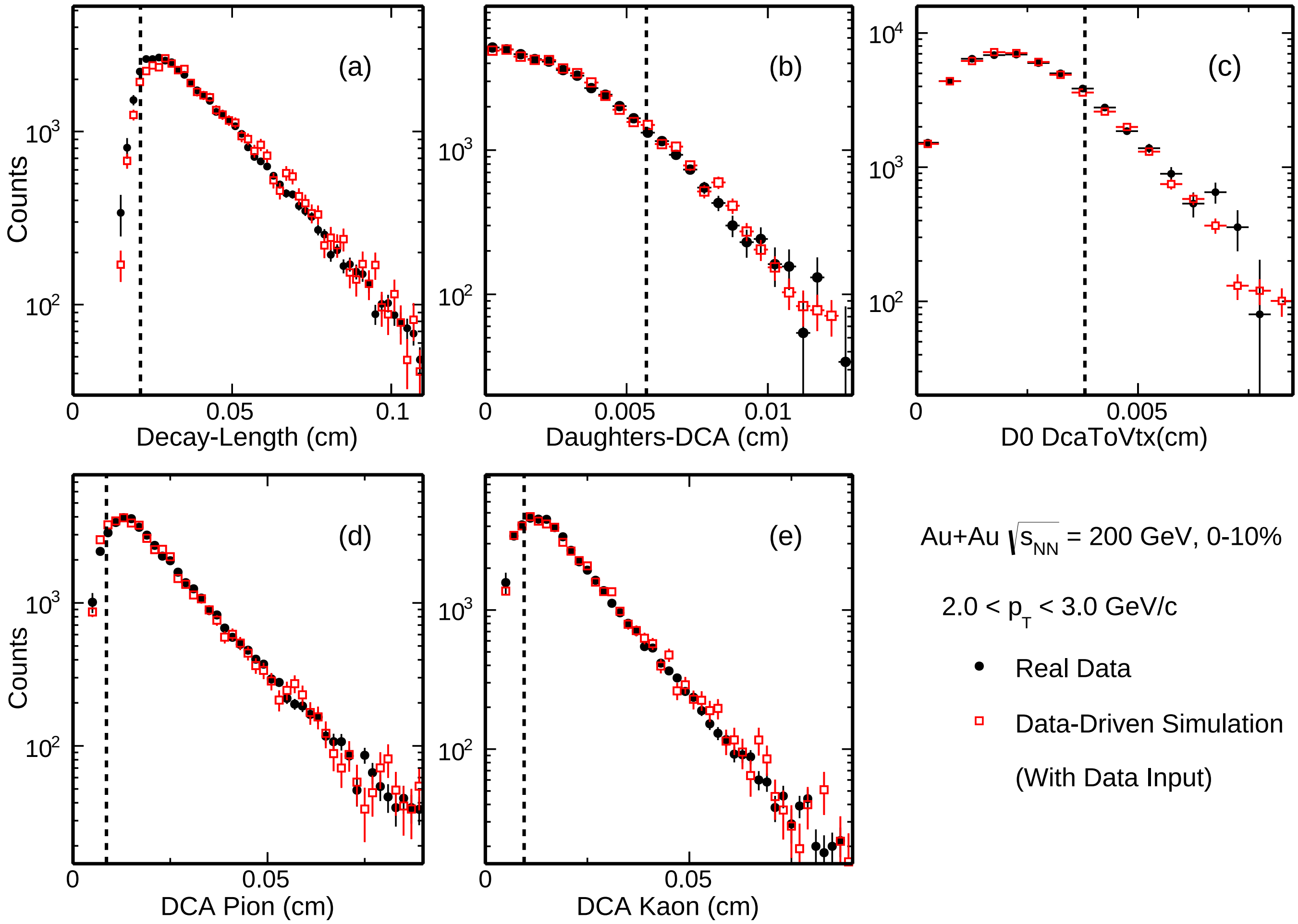

FIG. 13. Comparison of topological variable distributions between D^0 signals in real data (*black*) and in data-driven Simulation with real data distributions as the input (*red*) in 0–10% Au+Au collisions for D^0 mesons at $2 < p_T < 3\,\mathrm{GeV}/c$. The dashed lines indicate the final topological cuts chosen for each individual topological variable.

lisions for D^0 mesons at $2 < p_T < 3\,\mathrm{GeV}/c$. The real data distributions are extracted by reconstructing D^0 signals with the same reconstruction cuts as in Sec. III except for the interested topological variable to be compared and then statistically subtracting the background distributions using the side-band method. The cut on the interested topological variable is loosened, but need to have some pre-cuts to ensure reasonable D^0 signal reconstruction for the extraction of these topological variable distributions. These pre-cuts effectively reduce the low-end reach for several topological variables, e.g. the D^0 decay length. In the data-driven simulation method, charged pion and kaon HFT matching ratio and 2D DCA distributions are used as the input to calculate these topological variables for D^0 signals. Figure 13 shows that in the selected ranges, the data-driven simulation method reproduces topological variables distributions of D^0 signals, which supports that this method can be reliably used to calculate the topological cut efficiency.

Figure 14 shows the HFT tracking and topological cut efficiency $\varepsilon_{\mathrm{HFT}}$ as a function of D^0 p_T for different centrality bins obtained using the data-driven simulation method described in this section with the input distributions taken from the real data. The smaller efficiency seen in central collisions is in part because the HFT tracking efficiency is lower in higher occupancy central collisions, and in addition because we choose tighter topological cuts in central collisions for background suppression.

4. Secondary particle contribution

In the data-driven method for obtaining the efficiency correction, inclusive pion and kaon distributions are taken from real data as the input while the validation with GEANT simulation is performed with primary particles. There is a small amount of secondary particle contribution (e.g. weak decays from K_S^0 and Λ) to the measured inclusive charged pion tracks.

The impact of secondary particle contribution to the

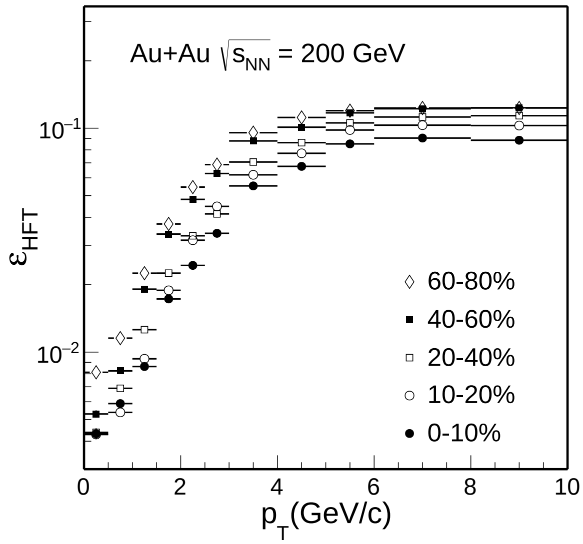

FIG. 14. D^0 HFT tracking and topological cut efficiencies $\varepsilon_{\mathrm{HFT}}$ from different centrality classes in Au+Au collisions at $\sqrt{s_{\mathrm{NN}}} = 200\,\mathrm{GeV}$.

charged pions is studied using the HIJING events processed through the GEANT simulation and the same offline reconstruction. The fraction of secondary pions from weak decay of strange hadrons (K_S^0 and Λ) to the total inclusive charged pions within DCA $< 1.5\,\mathrm{cm}$ cut is estimated to be around 5% at pion $p_T = 0.3\,\mathrm{GeV}/c$ and decrease to be $< 2\%$ above $2\,\mathrm{GeV}/c$. This is consistent with what was observed before in measuring the prompt charged pion spectra [26]. There is another finite contribution of low momentum anti-protons and anti-neutrons annihilated in the detector material and producing secondary pions. The transverse momenta of these pions are mostly around 2–3 GeV/c and the fraction of total inclusive pions is $\sim$ 10–12% at $p_T =$ 2-3 GeV/c based on this simulation and contribute $\sim$ 5–8% to the HFT matching ratio. This is obtained using the GEANT simulation with GHEISHA hadronic package. With a different hadronic package, FLUKA, the secondary pion fraction in 2–3 GeV/c region is significantly reduced to be negligible. The difference between the primary pions and the inclusive pions in the HFT matching efficiency has been considered as one additional correction factor in our data-driven simulation method when calculating the final efficiency. The maximum difference with respect to the result obtained using the GHEISHA hadronic package is included as the systematic uncertainty for this source. Figure 15 shows the secondary pion contribution in Au+Au collisions. Panel (a) shows the fraction of different sources for secondary tracks including the weak decays, the scattering and the $\bar{p}/\bar{n}$ annihilation in the detector material. Panel (b) shows the HFT matching efficiencies for inclusive, prompt and secondary pions. Panel (c) is the ratio of the HFT matching efficiencies between the inclusive and the primary pions from panel (b). The effect of such secondary contribution to charged kaons is found to be negligible [26].

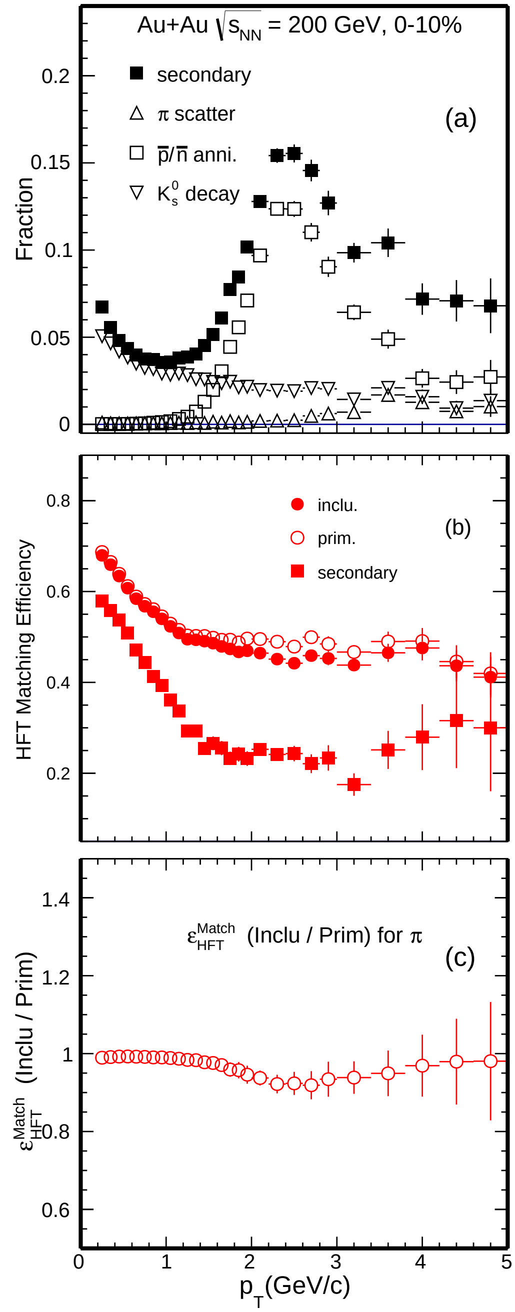

FIG. 15. Secondary pion contribution estimated from Hijing+GEANT simulation. Panel (a) shows the fraction of different sources for secondary pion tracks. Panel (b) shows the HFT matching efficiency $\varepsilon_{\mathrm{HFT}}^{\mathrm{match}}$ for inclusive, primary and secondary pions. Panel (c) shows the ratio of HFT matching efficiencies between inclusive and primary pions.

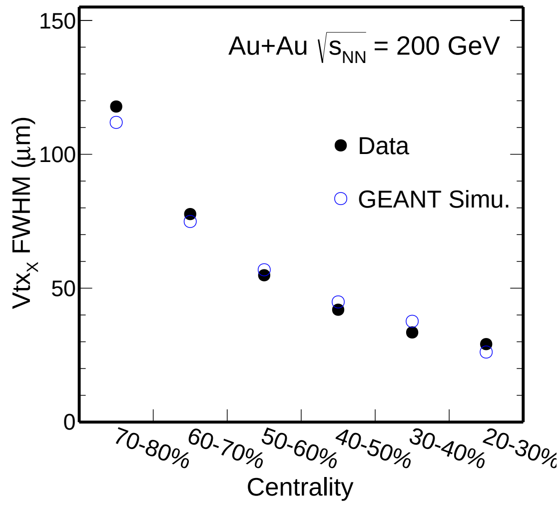

FIG. 16. Full-Width-at-Half-Maximum (FWHM) of vertex position difference in the X dimension between two randomly-divided sub-events in various centrality bins. Black solid circles present the FWHM values from real data while blue empty circles are from Hijing+GEANT simulation. Statistical uncertainties are smaller than the marker size.

C. Vertex Resolution Correction - $\varepsilon_{\rm vtx}$

In the data-driven approach, D^0 mesons are injected at the event vertex. In the real data, the reconstructed vertex has a finite resolution with respect to the real collision vertex. This may have some effect on the reconstructed D^0 signal counts after applying the topological cuts in small multiplicity events where the event vertex resolution decreases. We carry out similar simulation studies as described in Sec. IV B 1 for other centrality bins. Figure 16 shows the Full-Width-at-Half-Maximum (FWHM) of the difference in the vertex x-position of two randomly-divided sub-events in various centrality bins between data and MC simulation. We choose the FWHM variable here as the distributions are not particularly Gaussian. The MC simulation reproduces the vertex difference distributions seen in the real data reasonably well. This gives us confidence for using this MC simulation setup to evaluate the vertex resolution correction $\varepsilon_{\rm vtx}$.

To estimate the vertex resolution effect, we embed single PYTHIA $c\bar{c}$ event into a HIJING Au+Au event, and the whole event is passed through the STAR GEANT simulation followed by the same offline reconstruction as in the real data production. The PYTHIA $c\bar{c}$ events are pre-selected to have at least one $D^0 \to K^-\pi^+$ decay or its charge conjugate to enhance the statistics. Figure 17 shows the comparison in the obtained D^0 reconstruction efficiency between MC simulation (*black*) and data-driven simulation using reconstructed MC data as the input (*red*) for 20–30% (left), 50–60% (middle) and 70–80% (right) centrality bins, respectively. The bottom panels show the ratios of the efficiencies obtained from the two calculation methods. In central and mid-central collisions, the data-driven simulation method can properly reproduce the D^0 real reconstruction efficiency. This is expected since the vertex resolution is small enough so that it has negligible impact on the obtained efficiency using the data-driven simulation method. However, in more peripheral collisions, the data-driven simulation method overestimates the D^0 reconstruction efficiency as shown in the middle and right panels. The vertex resolution correction factor $\varepsilon_{\rm vtx}$, denotes in Equ. 3, has a mild p_T (2 and 4 GeV/c) dependence but strong centrality dependence as shown in Fig. 18. The brackets denote the systematic uncertainties in the obtained correction factor $\varepsilon_{\rm vtx}$. They are estimated by varying the multiplicity range in the HIJING + GEANT simulation so that the sub-event vertex difference distributions in the real data can be covered by distributions obtained from different simulation samples. The vertex resolution corrections are applied as a function of p_T in each individual centrality class.

D. PID Efficiency - $\varepsilon_{\rm PID}$ and Doubly-mis-PID Correction

The D^0 daughter particle identification (PID) cut efficiency includes contributions from the dE/dx selection cut efficiency as well as the TOF matching and $1/\beta$ cut efficiency. To best estimate the selection cut efficiency, we select the enriched kaon and pion samples from ϕ, K_S^0 decays following the same procedure as in [27, 28] and obtain the mean and width in the dE/dx $n\sigma_X$ distributions. The dE/dx cut efficiencies for pion and kaon daughter tracks are calculated respectively. The TOF $1/\beta$ cut efficiency is determined by studying the $1/\beta$ distributions for kaons and pions in the clean separation region, namely $p_T < 1.5\,{\rm GeV}/c$. There is a mild dependence for the offset and width of $\Delta 1/\beta$ distributions vs. particle momentum and our selection cuts are generally wide enough to capture nearly all tracks once they have valid β measurements. The total PID efficiency of D^0 mesons is calculated by folding the individual track TPC and TOF PID efficiencies following the same hybrid PID algorithm as implemented in the data analysis. Figure 19 shows the total PID efficiencies for D^0 reconstruction in various centrality bins. The total PID efficiency is generally high and has nearly no centrality or p_T dependence.

When the D^0 daughter kaon track is mis-identified as a pion track and the other daughter pion track is mis-identified as a kaon track, the pair invariant mass distribution will have a bump structure around the real D^0 signal peak, but the distribution is much broader in a wide mass region due to the mis-assigned daughter particle masses. Based on the PID performance study described above, we estimate the single kaon and pion candidate track purities. After folding the realistic particle momentum resolution, we calculate the reconstructed D^0

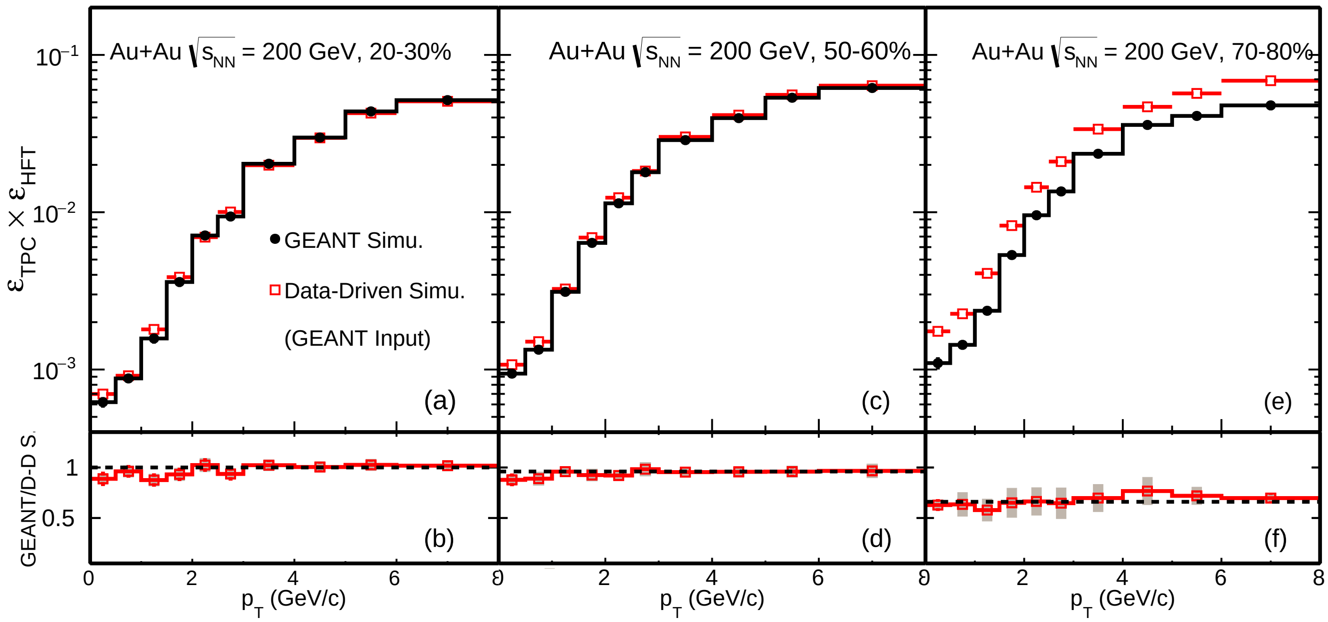

FIG. 17. D^0 reconstruction efficiency comparison between MC GEANT simulation (GEANT, *black*) and data-driven simulation with the reconstructed MC data as the input (D-D S.,*red*) for 20–30% (a), 50–60% (c) and 70–80% (e) Au+Au collisions. Bottom panels (b,d,f) show the ratios between the two distributions above.

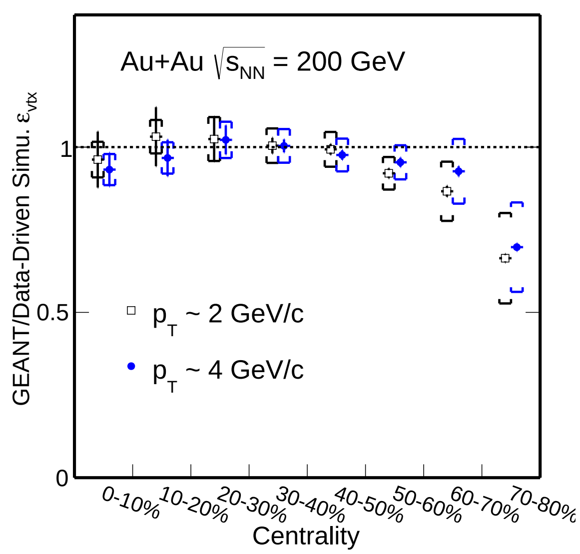

FIG. 18. $\varepsilon_{\rm vtx}$, D^0 reconstruction efficiency ratios between MC GEANT simulation and data-driven simulation with the reconstructed MC data as the input versus collision centrality for p_T at 2 and 4 GeV/c. The brackets depict the estimated systematic uncertainties.

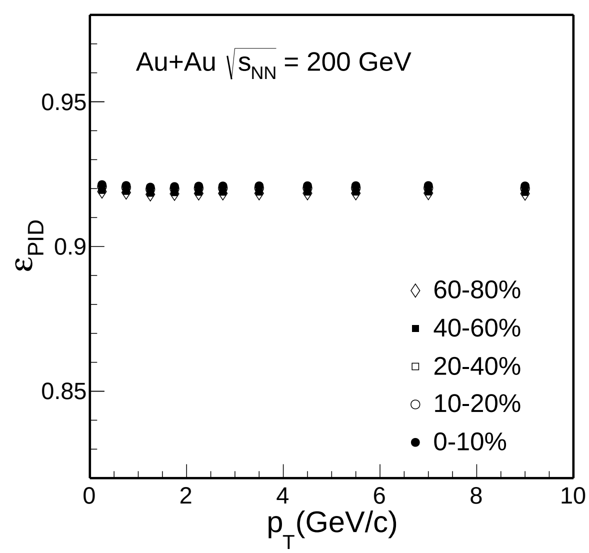

FIG. 19. Particle identification efficiency ($\varepsilon_{\rm PID}$) of D^0 mesons in different centrality classes.

yield from doubly mis-identified pairs (double counting) underneath the real D^0 signal and the double counting fraction is shown in Fig. 20. The black markers show the fraction by taking all doubly mis-identified pairs in the D^0 mass window while the blue markers depict it with an additional side-band (SB) subtraction. The latter is used as a correction factor to the central values of reported D^0 yields while the difference between the black and blue symbols is considered as the systematic uncertainty in this source. The double counting fraction is below 10% in all p_T bins, and there is little centrality dependence.

Figure 21 shows the total D^0 reconstruction efficiency from different centrality classes in Au+Au collisions including all of the individual components discussed above.

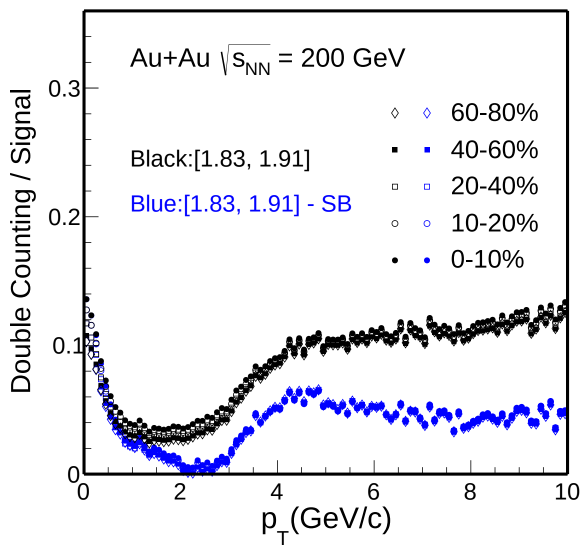

FIG. 20. D^0 yield double counting fraction due to doubly mis-PID in different centrality classes. The black markers depict an estimation taking the total double counting yield in the D^0 mass window while the blue markers depict an estimation with an additional side-band (SB) subtraction. Note that most data points from different centrality bins overlap with each other.

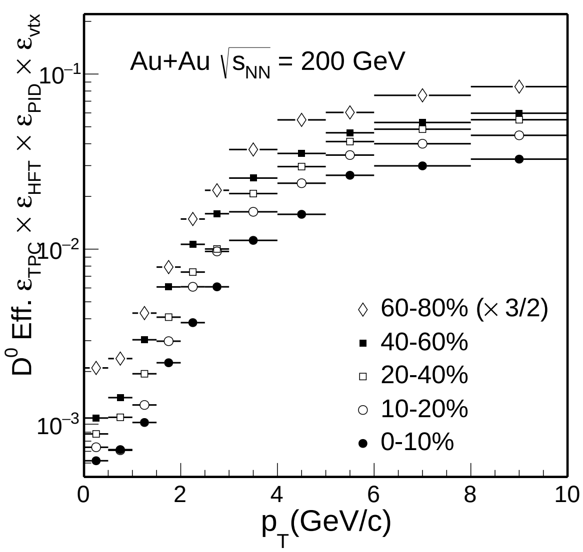

FIG. 21. The total D^0 reconstruction efficiency from different centrality classes.

V. SYSTEMATIC UNCERTAINTIES

The systematic uncertainty on the final measured D^0 p_T spectra can be categorized as the uncertainty of the raw D^0 yield extraction and the uncertainty of efficiencies and corrections.

The uncertainty of the raw yield extraction is estimated by a) the difference in the D^0 yield obtained with the fit and bin counting methods, b) varying invariant mass ranges for fit and for side bands and c) varying background estimation from mixed-event and like-sign methods. The maximum difference between these scenarios is then converted to the standard deviation and added to the systematic uncertainties. It is the smallest in the mid-p_T bins due to the best signal significance and grows at both low and high p_T. The double counting contribution in the D^0 raw yield due to mis-PID is included as another contribution to the systematic uncertainty for the D^0 raw yield extraction as described in Sec. IV D.

The uncertainty of the TPC acceptance and efficiency correction $\varepsilon_{\rm TPC}$ is estimated via the standard procedure in STAR by comparing the TPC track distributions between real data and the embedding data. It is estimated to be ∼5–7% for 0–10% collisions and ∼5–8% for 60–80% collisions, and is correlated for different centralities and p_T regions.

The uncertainty of the PID efficiency correction is estimated by varying the PID selection cuts and then convolute to the final corrected D^0 yield.

To estimate the uncertainty of the HFT tracking and topological cut efficiency correction $\varepsilon_{\rm HFT}$, we employ the following procedures: a) We vary the topological variable cuts so the D^0 $\varepsilon_{\rm HFT}$ is changed to 50% and 150% of the nominal (default) efficiency and compare the efficiency corrected final D^0 yields. The maximum difference between the two scenarios is then added to the systematic uncertainties. b) We also vary the daughter p_T low threshold cut between 0.3 to 0.6 GeV/c and the maximum difference in the final corrected D^0 yield is also included in the systematic uncertainties. c) We add the systematic uncertainty due to limitation of the data-driven simulation approach, ∼5%, and the impact of the secondary particles, ∼2%, to the total $\varepsilon_{\rm HFT}$ systematic uncertainty.

With the corrected D^0 transverse momentum spectra, the nuclear modification factor $R_{\rm CP}$ is calculated as the ratio of $N_{\rm bin}$ normalized yields between central and peripheral collisions, as shown in the following formula:

$$R_{\rm CP} = \frac{d^2N/dp_Tdy}{N_{\rm bin}}\Big|_{\rm cen} \times \frac{N_{\rm bin}}{d^2N/dp_Tdy}\Big|_{\rm peri}. \qquad (4)$$

The systematic uncertainties in the raw signal extraction in central and peripheral collisions are propagated as they are uncorrelated, while systematic uncertainties in many other sources are correlated or partially correlated in contributing to the measured D^0 yields. To best consider these correlations, we vary different variables simultaneously in central and peripheral collisions, and the difference in the final extracted $R_{\rm CP}$ value is then directly counted as systematic uncertainties in the measured $R_{\rm CP}$.

The nuclear modification factor $R_{\rm AA}$ is calculated as the ratio of $N_{\rm bin}$ normalized yields between Au+Au and p+p collisions. The baseline for p+p collisions is chosen the same as the publication [12]. The uncertainties from the p+p reference dominates the systematic uncertainty for R_{AA}. They include the 1σ uncertainty from the Levy function fit to the measured spectrum and the difference between Levy and power-law function fits for extrapolation to low and high p_T, expressed as one standard deviation.

With the corrected D^0 and $\overline{D}^0$ transverse momentum spectra, the $\overline{D}^0/D^0$ ratio is calculated as a function of the transverse momentum. The systematic uncertainties in the raw signal extraction for $\overline{D}^0$ and D^0 are propagated as they are uncorrelated, while systematic uncertainties in many other sources are correlated or partially correlated in contributing to the measured $\overline{D}^0/D^0$ ratio. As in the R_{CP} systematic uncertainty estimation, we vary different variables simultaneously for D^0 and $\overline{D}^0$, and the difference in the final extracted $\overline{D}^0/D^0$ value is then directly counted as systematic uncertainties in the measured $\overline{D}^0/D^0$.

Table V summarizes the systematic uncertainties and their contributions, in percentage, on the D^0 invariant yield in 0–10% and 60–80% collisions and R_{CP}(0–10%/60–80%). In the last column we also comment on the correlation in p_T for each individual source. Later when reporting p_T integrated yields or R_{CP}, systematic uncertainties are calculated under the following considerations: a) for p_T uncorrelated sources, we take the quadratic sum of various p_T bins; b) for sources that are largely correlated in p_T, we take the arithmetic sum as a conservative estimate.

VI. RESULTS AND DISCUSSION

A. p_T Spectra and Integrated Yields

Figure 22 shows the efficiency corrected D^0 invariant yield at mid-rapidity ($|y| < 1$) vs. p_T in 0–10%, 10–20%, 20–40%, 40–60% and 60–80% Au+Au collisions. D^0 spectra in some centrality bins are arbitrarily scaled with factors indicated on the plot for clarity. Dashed and solid lines depict fits to the spectra with the Levy function:

$$\begin{aligned}\frac{d^2N}{2\pi p_T dp_T dy} =& \frac{1}{2\pi}\frac{dN}{dy}\frac{(n-1)(n-2)}{nT(nT+m_0(n-2))} \\ &\times\left(1+\frac{\sqrt{p_T^2+m_0^2}-m_0}{nT}\right)^{-n},\end{aligned} \tag{5}$$

where m_0 is the D^0 mass (1.864 GeV/c^2) and dN/dy, T and n are free parameters. The Levy function fit describes the D^0 spectra nicely in all centrality bins up to $8\,\mathrm{GeV}/c$.

We compare our new measurements with previous measurements using the STAR TPC only. The previous measurements are recently corrected after fixing errors in the TOF PID efficiency calculation [12]. Figure 23 shows the p_T spectra comparison in 0–10%, 10-40% and 40–80% centrality bins in panel (a) and the ratios to the Levy fit functions in panels (b), (c), and (d), respectively. The new measurement with the HFT detector shows a nice agreement with the measurement without the HFT, but with significantly improved precision.

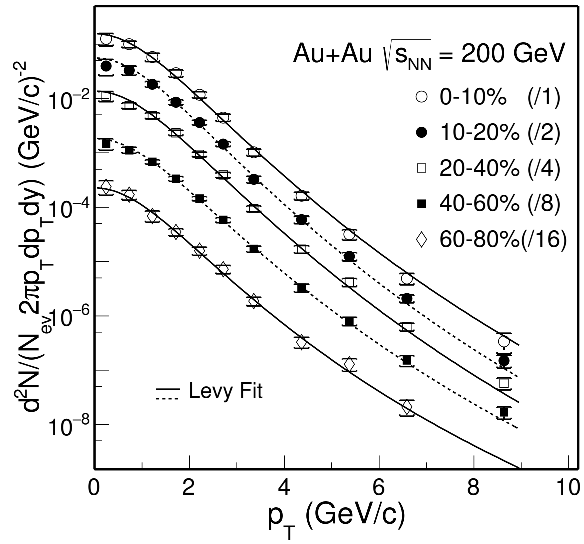

FIG. 22. D^0 invariant yield at mid-rapidity ($|y| < 1$) vs. transverse momentum for different centrality classes. Error bars (not visible for many data points) indicate statistical uncertainties and brackets depict systematic uncertainties. Global systematic uncertainties in $B.R.$ are not plotted. Solid and dashed lines depict Levy function fits.

The measured D^0 spectra cover a wide p_T region which allows us to extract the p_T integrated total D^0 yield at mid-rapidity with good precision. Figure 24 shows the p_T integrated cross section for D^0 production per nucleon-nucleon collision $d\sigma^{NN}/dy|_{y=0}$ from different centrality bins for the full p_T range shown in the top panel and for $p_T > 4\,\mathrm{GeV}/c$ shown in the bottom panel. The result from the previous p+p measurement is also shown in the top panel [20].

The total D^0 cross section per nucleon-nucleon collision at mid-rapidity $d\sigma^{NN}/dy|_{y=0}$ in Au+Au collisions shows approximately a flat distribution as a function of N_{part}, though the systematic uncertainty in the 60–80% centrality bin is a bit large. The values in mid-central to central Au+Au collisions are smaller than that in p+p collisions with $\sim 1.5\sigma$ effect considering the large uncertainties from the p+p measurements. The total charm quark yield in heavy-ion collisions is expected to follow the number-of-binary-collision scaling since charm quarks are believed to be predominately created at the initial hard scattering before the formation of the QGP at RHIC energies. However, the cold nuclear matter (CNM) effect including shadowing could also play an important role. In addition, hadronization through coalescence has been suggested to potentially modify the charm quark distribution in various charm hadron states which may lead to

TABLE V. Summary of systematic uncertainties, in percentage, on the D^0 invariant yield in 0–10% and 60–80% collisions and R_{CP}(0–10%/60–80%).

Source	Systematic uncertainty [%]			Correlation in p_T
	0–10%	60–80%	R_{CP}(0–10%/60–80%)	
Signal extra.	1-6	1-12	2-13	uncorr.
Double mis-PID	1-7	1-7	negligible	uncorr.
$\varepsilon_{\mathrm{TPC}}$	5-7	5-8	3-7	largely corr.
$\varepsilon_{\mathrm{HFT}}$	3-15	3-20	3-20	largely corr.
$\varepsilon_{\mathrm{PID}}$	3	3	negligible	largely corr.
$\varepsilon_{\mathrm{vtx}}$	5	9-18	10-18	largely corr.
BR.	0.5		0	global
N_{bin}	2.8	42	42	global

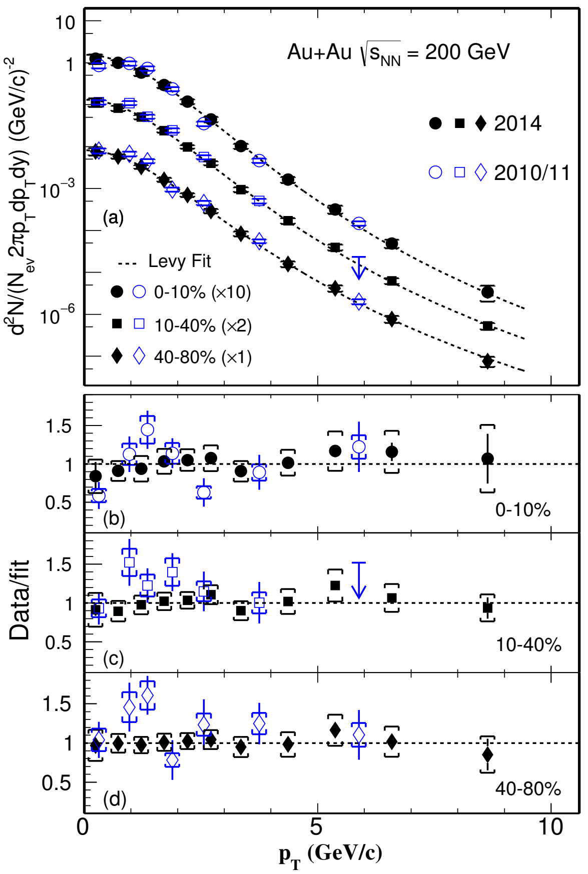

FIG. 23. (a) Measured D^0 spectra from this analysis compared with the previous 2010/11 measurements for different centrality classes. Dashed lines depict Levy function fits to 2014 data. (b) - (d), Ratio of measured spectra to the fitted Levy functions in 0–10%, 10–40% and 40–80% centrality bins, respectively.

the reduction in the observed D^0 yields in Au+Au collisions [29] (as seen in Fig. 24). For instance, hadronization through coalescence can lead to an enhancement of the charmed baryon Λ_c^+ yield relative to D^0 yield [30], and together with the strangeness enhancement in the hot QCD medium, can also lead to an enhancement in the charmed strange meson D_s^+ yield relative to D^0 [31]. Therefore, determination of the total charm quark yield in heavy-ion collisions will require measurements of other charm hadron states over a broad momentum range.

B. Collectivity

1. m_{T} Spectra

Transverse mass spectra can be used to study the collectivity of produced hadrons in heavy-ion collisions. Figure 25 shows the D^0 invariant yield at mid-rapidity ($|y|<1$) vs. transverse kinetic energy (m_T-m_0) for different centrality classes, where $m_T = \sqrt{p_T^2 + m_0^2}$ and m_0 is the D^0 meson mass. Solid and dashed black lines depict thermal model inspired exponential function fits to data in various centrality bins up to $m_T - m_0 < 3\,\mathrm{GeV}/c^2$ using the fit function shown below:

$$\frac{d^2N}{2\pi m_T dm_T dy} = \frac{dN/dy}{2\pi T_{\mathrm{eff}}(m_0 + T_{\mathrm{eff}})} e^{-(m_T - m_0)/T_{\mathrm{eff}}}. \quad (6)$$

Such a method has been often used to analyze the particle spectra and to understand kinetic freeze-out properties for the data in heavy–ion collisions [1, 32].

A power-law function (shown below) is also used to fit the spectrum in the 60–80% centrality bin:

$$\frac{d^2N}{2\pi p_T dp_T dy} = \frac{dN}{dy}\frac{4(n-1)(n-2)}{2\pi(n-3)^2\langle p_T\rangle^2}\left(1 + \frac{2p_T}{\langle p_T\rangle(n-3)}\right)^{-n}, \quad (7)$$

where dN/dy, $\langle p_T\rangle$, and n are three free parameters.

The power-law function fit shows a good description of the 60–80% centrality data indicating that the D^0 meson production in this peripheral bin is close to the expected feature of perturbative QCD. The D^0 meson spectra in more central collisions can be well described by the exponential function fit at $m_T - m_0 < 3\,\mathrm{GeV}/c^2$ suggesting the D^0 mesons have gained collective motion in the medium evolution in these collisions.

The obtained slope parameter T_{eff} for D^0 mesons is compared to other light and strange hadrons measured

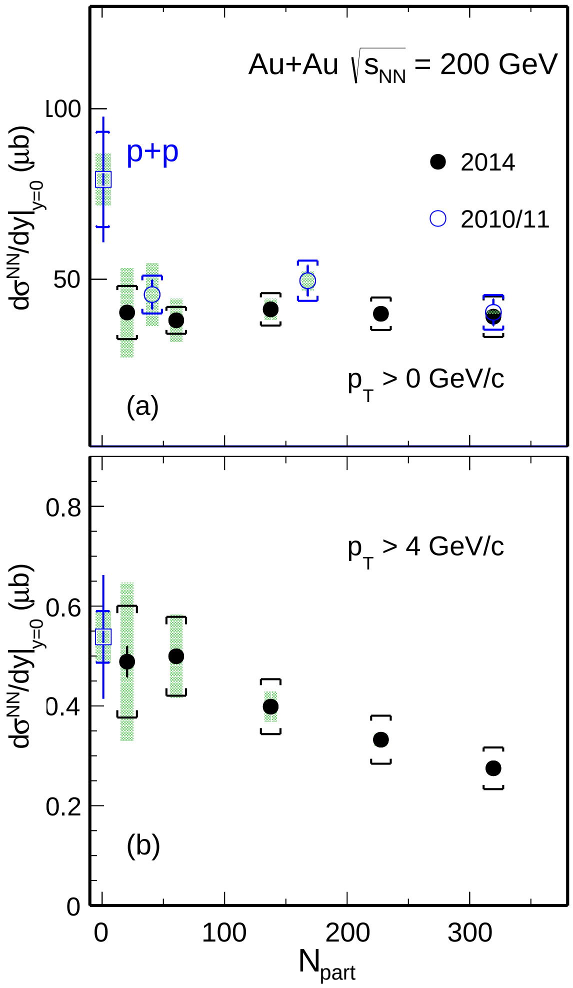

FIG. 24. Integrated D^0 cross section per nucleon-nucleon collision at mid-rapidity for $p_T > 0$ (a) and $p_T > 4\,\mathrm{GeV}/c$ (b) as a function of centrality N_{part}. The statistical and systematic uncertainties are shown as error bars and brackets on the data points. The green boxes on the data points depict the overall normalization uncertainties in p+p and Au+Au data respectively.

at RHIC. Figure 26 summarizes the slope parameter T_{eff} for various identified hadrons ($\pi^{\pm}$, $K^{\pm}$, $p/\bar{p}$, ϕ, Λ, Ξ^-, Ω, D^0 and J/ψ) in central Au+Au collisions at $\sqrt{s_{\mathrm{NN}}} = 200\,\mathrm{GeV}$ [26, 33–35]. Point-by-point statistical and systematic uncertainties are added as a quadratic sum when performing these fits. All fits are performed up to $m_T - m_0 < 1\,\mathrm{GeV}/c^2$ for π, K, p, $< 2\,\mathrm{GeV}/c^2$ for ϕ, Λ, Ξ, and $< 3\,\mathrm{GeV}/c^2$ for Ω, D^0, J/ψ, respectively.

The slope parameter T_{eff} in a thermalized medium can be characterized by the random (generally interpreted as a kinetic freeze-out temperature T_{fo}) and collective (radial flow velocity $\langle\beta_T\rangle$) components with a simple relation [1, 36, 37]:

$$T_{\mathrm{eff}} = T_{\mathrm{fo}} + m_0\langle\beta_T\rangle^2, \tag{8}$$

therefore, T_{eff} will show a linear dependence as a function

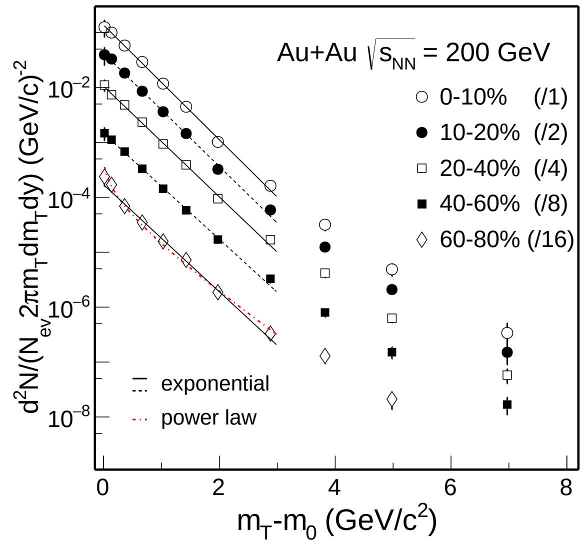

FIG. 25. D^0 invariant yield at mid-rapidity ($|y| < 1$) vs. transverse kinetic energy (m_T-m_0) for different centrality classes. Error bars (not visible for many data points) indicate statistical uncertainties and brackets depict systematic uncertainties. Global systematic uncertainties in $B.R.$ are not plotted. Solid and dashed black lines depict exponential function fits and the dot-dashed line depict a power-law function fit to the spectrum in 60–80% centrality bin.

of particle mass m_0 with a slope that can be used to characterize the radial flow collective velocity.

The data points clearly show two different systematic trends. π, K, p data points follow one linear dependence while ϕ, Λ, Ξ^-, Ω^-, D^0 data points follow another linear dependence, as represented by the dashed lines shown in Fig. 26. Particles, such as, π, K, p gain radial collectivity through the whole system evolution, therefore the linear dependence exhibits a larger slope. On the other hand the linear dependence of ϕ, Λ, Ξ^-, Ω^-, D^0 data points shows a smaller slope indicating these particles may freeze out from the system earlier, and therefore receive less radial collectivity.

2. *Blast-wave fit*

The Blast-Wave (BW) model is extensively used to study the particle kinetic freeze-out properties [26, 38]. Assuming a hard-sphere uniform particle source with a kinetic freeze-out temperature T_{kin} and a transverse radial flow velocity β, the particle transverse momentum spectral shape is given by [39]:

$$\frac{dN}{p_T dp_T} = \frac{dN}{m_T dm_T} \propto \int_0^R r dr m_T I_0\left(\frac{p_T \sinh\rho}{T_{\mathrm{kin}}}\right) K_1\left(\frac{m_T \cosh\rho}{T_{\mathrm{kin}}}\right), \tag{9}$$

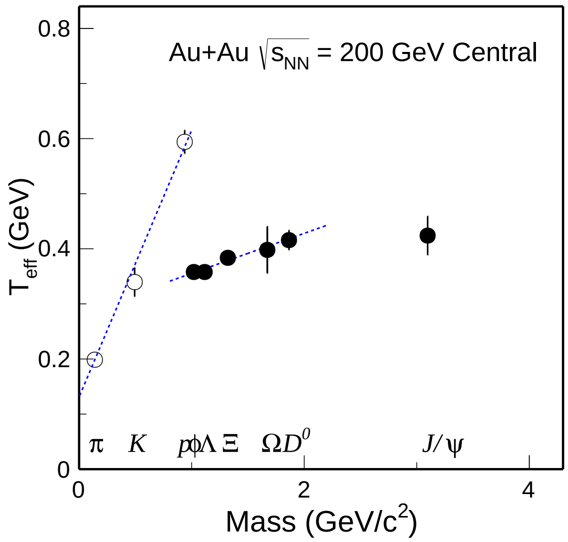

FIG. 26. Slope parameter $T_{\rm eff}$ for different particles in central Au+Au collisions [26, 33–35]. The dashed lines depict linear function fits to π, K, p and $\phi, \Lambda, \Xi^-, \Omega^-, D^0$ respectively.

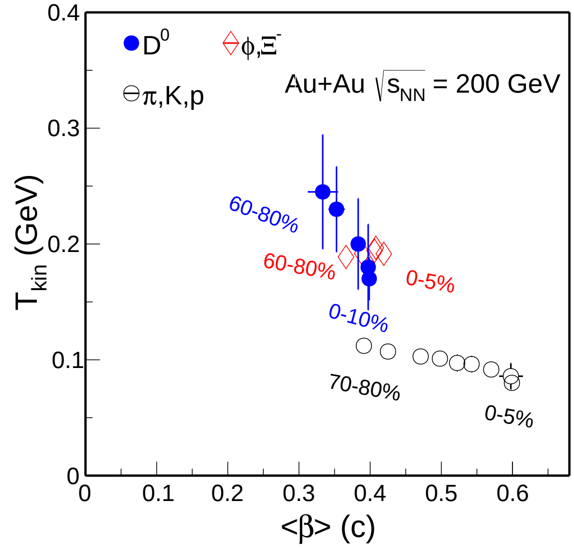

FIG. 28. Results of $T_{\rm kin}$ vs. $\langle\beta\rangle$ from the Blast-Wave model fits to different groups of particles. The data points for each group of particles present the results from different centrality bins with the most central data point at the largest $\langle\beta\rangle$.

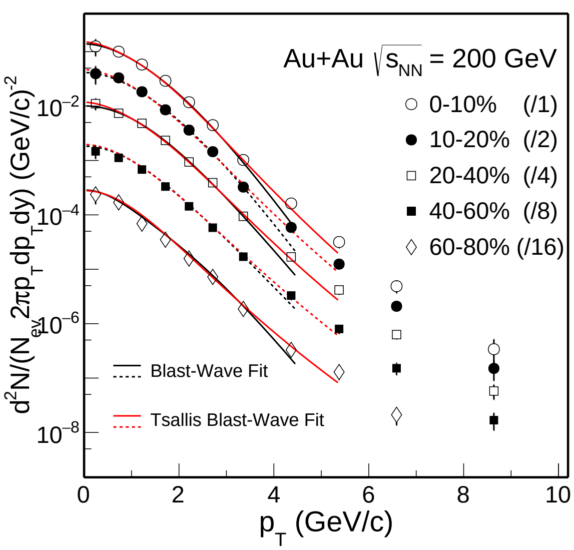

FIG. 27. D^0 invariant yield at mid-rapidity ($|y|<1$) vs. transverse momentum for different centrality classes. Black and red lines depict Blast-Wave (BW) and Tsallis Blast-Wave (TBW) fits for each centrality bin respectively.

where $\rho = \tanh^{-1}\beta$, and I_0 and K_1 are the modified Bessel functions. The flow velocity profile is taken as:

$$\beta = \beta_s \left(\frac{r}{R}\right)^n, \tag{10}$$

where β_s is the maximum velocity at the surface and r/R is the relative radial position in the thermal source. The choice of R only affects the overall spectrum magnitude while the spectrum shape constrains the three free parameters $T_{\rm kin}$, $\langle\beta\rangle = 2/(2+n)\beta_s$, and n.

Figure 27 shows the Blast-Wave and Tsallis Blast-Wave (TBW) fits to the data in different centrality bins. The n parameter in these fits are fixed to be 1 due to the limited number of data points and is inspired by the fit result for light-flavor hadrons (π, K, p) [40]. The p_T range in the BW fits is restricted to be less than $3m_0$ where m_0 is the rest mass of D^0 mesons.

Figure 28 summarizes the fit parameters $T_{\rm kin}$ vs. $\langle\beta\rangle$ from the Blast-Wave model fits to different groups of particles: black markers for the simultaneous fit to π, K, p; red markers for the simultaneous fit to ϕ, Ξ^- and blue markers for the fit to D^0. The data points for each group of particles represent the fit results from different centrality bins with the most central data point at the largest $\langle\beta\rangle$ value. Similar as in the fit to the m_T spectra, point-by-point statistical and systematic uncertainties are added in quadrature when performing the fit. The fit results for π, K, p are consistent with previously published results [40]. The fit results for multi-strangeness particles ϕ, Ξ^- and D^0 show much smaller mean transverse velocity $\langle\beta\rangle$ and larger kinetic freeze-out temperature, suggesting these particles decouple from the system earlier and gain less radial collectivity compared to light hadrons. The resulting $T_{\rm kin}$ parameters for ϕ, Ξ^- and for D^0 are close to the pseudocritical temperature T_c calculated from a lattice QCD calculation at zero baryon chemical potential [41], indicating negligible contribution from the hadronic stage to the observed radial flow of these particles. Therefore the collectivity that D^0 mesons obtain is mostly through the partonic stage re-scatterings in the QGP phase.

The TBW fit accounts for non-equilibrium features in a system with an additional parameter q [40]. Table VI lists

TABLE VI. $\langle\beta\rangle$ and $(q-1)$ from the Tsallis Blast-Wave fits to the D^0 data in different centralities .

Centrality	$\langle\beta\rangle(c)$	$q-1$
0–10 %	0.263 ± 0.018	0.066 ± 0.008
10–20 %	0.255 ± 0.022	0.068 ± 0.010
20–40 %	0.264 ± 0.015	0.070 ± 0.007
40–60 %	0.251 ± 0.023	0.074 ± 0.011
60–80 %	0.217 ± 0.037	0.075 ± 0.010

the fitting parameters, $\langle\beta\rangle$ and $(q-1)$ for the D^0 data in different centralities. Results show a similar trend as the regular BW fit, i.e. the most central data point is located at the largest $\langle\beta\rangle$ value. The $(q-1)$ parameter in TBW, which characterizes the degree of non-equilibrium in a system, is found to be close to zero, indicating that the system is approaching thermalization in these collisions.

C. Nuclear Modification Factor - $R_{\rm CP}$ and $R_{\rm AA}$

Figure 29 shows the calculated $R_{\rm CP}$ with the 60–80% peripheral bin as the reference for different centrality bins 0–10%, 10–20%, 20–40% and 40–60% and the results are compared to other light and strange flavor mesons. The grey bands around unity depict the vertex resolution correction uncertainty on the measured D^0 data points, mostly originating from the 60–80% reference spectrum. The dark and light green boxes around unity on the right side indicate the global $N_{\rm bin}$ systematic uncertainties for the 60–80% centrality bin and for the corresponding centrality bin in each panel. The global $N_{\rm bin}$ systematic uncertainties should be applied to the data points of all particles in each panel.

The measured D^0 $R_{\rm CP}$ in central 0–10% collisions shows a significant suppression at $p_T > 5\,{\rm GeV}/c$. The suppression level is similar to that of light and strange flavor mesons and the $R_{\rm CP}$ suppression gradually decreases when moving from central collisions to mid-central and peripheral collisions. The D^0 $R_{\rm CP}$ for $p_T < 4\,{\rm GeV}/c$ is consistent with no suppression, in contrast to light-flavor hadrons. This structure is consistent with the expectation from model predictions that charm quarks gain sizable collective motion during the medium evolution. Comparisons to dynamic model calculations for the D^0 $R_{\rm CP}$ will be discussed in the next Sec. VI E.

The precision of the 60–80% centrality spectrum is limited due to the large systematic uncertainty in determining the $N_{\rm bin}$ based on the MC Glauber model. Figure 30 shows the D^0 $R_{\rm CP}$ for different centralities as a function of p_T with the 40–60% centrality spectrum as the reference. The grey bands around unity in the each panel represent the systematic uncertainties due to the vertex resolution contribution from the 40–60% centrality. The green boxes around unity depict the global $N_{\rm bin}$ systematic uncertainties for the 40–60% centrality bin and for each corresponding centrality bin. As a comparison, $R_{\rm CP}$ of charged pions, K^0_s and ϕ in the corresponding centralities are also plotted in each panel. With much smaller systematic uncertainties, the observations seen before using the 60–80% centrality spectrum as the reference still hold.

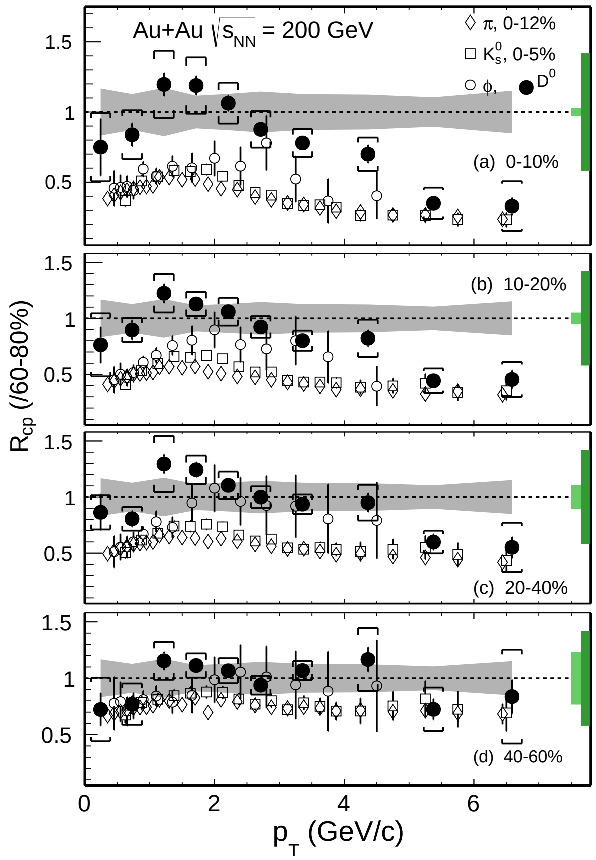

FIG. 29. D^0 $R_{\rm CP}$ with the 60–80% spectrum as the reference for different centrality classes in Au+Au collisions compared to that of other light and strange mesons ($\pi^\pm$, K^0_S and ϕ) [42–44]. The statistical and systematic uncertainties are shown as error bars and brackets on the data points. The grey bands around unity depict the systematic uncertainty due to vertex resolution correction, mostly from the 60–80% reference spectrum. The light and dark green boxes on the right depict the normalization uncertainties in determining the $N_{\rm bin}$ for each centrality (light green) and the 60–80% centrality bin (dark green), respectively.

Figure 31 shows the calculated $R_{\rm AA}$ with the p+p measurement [20] as the reference for different centrality bins 0–10% (a), 10–40% (b) and 40–80% (c), respectively. The new $R_{\rm AA}$ measurements are also compared to the previous Au+Au measurements using the STAR TPC after the recent correction [12]. The p+p D^0 reference spectrum is updated using the latest global analysis of charm fragmentation ratios from [48] and also by taking into account the p_T dependence of the fragmentation ratio between D^0 and $D^{*\pm}$ from PYTHIA. The new measurement with the HFT detector shows a nice agreement with the measurement without the HFT, but with much im-

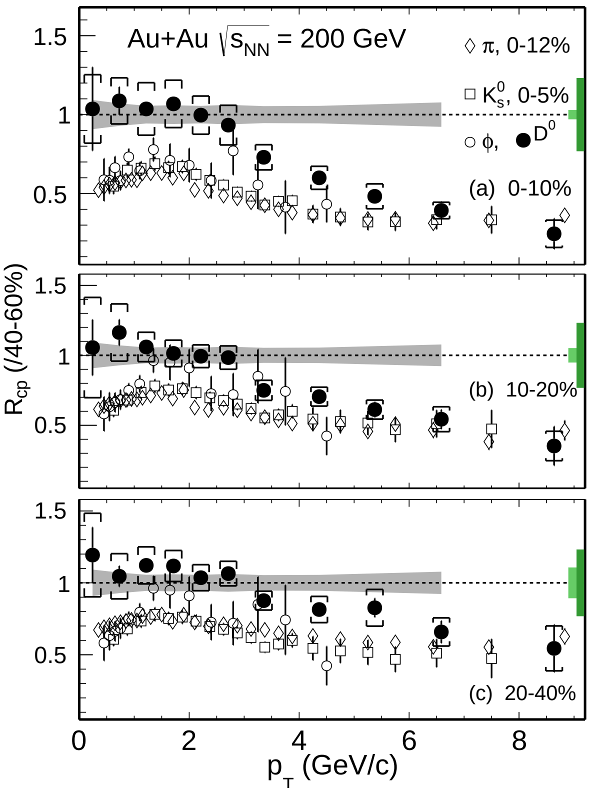

FIG. 30. D^0 $R_{\rm CP}$ with the 40–60% spectrum as the reference for different centrality classes in Au+Au collisions compared to that of other light and strange mesons ($\pi^{\pm}$, K^0_S and ϕ) [42–44]. The statistical and systematic uncertainties are shown as error bars and brackets on the data points. The grey bands around unity depict the systematic uncertainty due to vertex resolution correction, mostly from the 40–60% reference spectrum. The light and dark green boxes on the right depict the normalization uncertainties in determining the $N_{\rm bin}$ for each centrality (light green) and the 40–60% centrality bin (dark green), respectively.

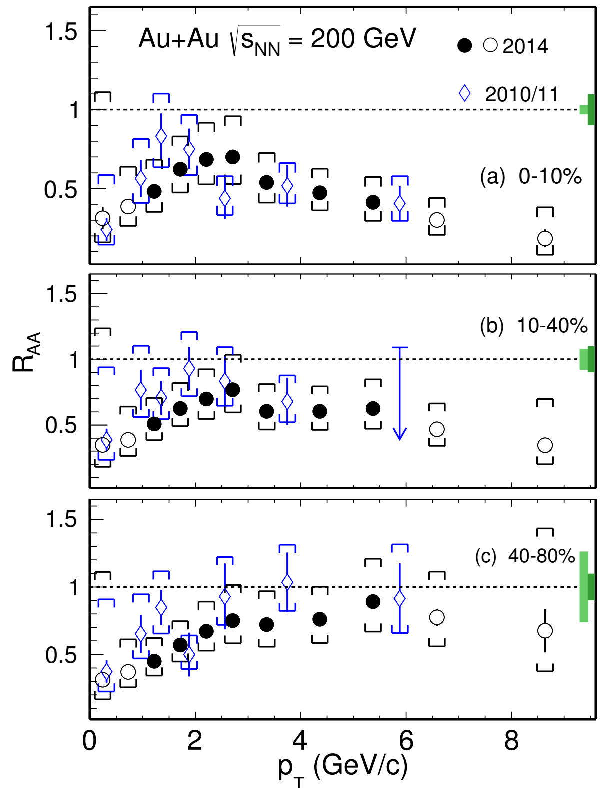

FIG. 31. D^0 $R_{\rm AA}$ in Au+Au collisions at $\sqrt{s_{\rm NN}} = 200$ GeV for 0–10% (a), 10–40% (b) and 40–80% (c) centrality bins, respectively. The first two and last two data points are presented as empty circles, indicating that the p+p reference is extrapolated into these p_T ranges. The statistical and systematic uncertainties are shown as error bars and brackets on the data points. The light and dark green boxes on the right depict the normalization uncertainties in determining the $N_{\rm bin}$ in Au+Au collisions and the total inelastic cross section in p+p collisions, respectively.

proved precision. The grey bands around each data point depict the p+p systematic uncertainty on the measured D^0 data points. The first two and last two data points are empty circles indicating those are calculated with an extrapolated p+p reference. The dark and light green boxes around unity on the right side indicate the global $N_{\rm bin}$ systematic uncertainties for the corresponding centrality bin in each panel and the total inelastic cross section uncertainty in p+p collisions.

The measured D^0 $R_{\rm AA}$ in central (0–10%) and mid-central (10–40%) collisions show a significant suppression at the high p_T range which reaffirms the strong interactions between charm quarks and the medium, while the new Au+Au data points from this analysis contain much improved precision. Figure 32 shows the D^0 $R_{\rm AA}$ in the 0–10% most central collisions compared to that of (a) average D-meson from ALICE and (b) charged hadrons from ALICE and $\pi^{\pm}$ from STAR [10, 49, 50]. The comparison of D^0 suppression between STAR and ALICE shows a reasonable agreement within the uncertainties despite of the large energy difference from 200 GeV to 2.76 TeV. The comparison to that of light hadrons shows a similar suppression at high p_T, while in the intermediate range, D^0 mesons seem to be less suppressed. The large uncertainty in the p+p baseline need to be further reduced before making more quantitative conclusions.

D. $\overline{D}^0$ and D^0 spectra and double ratio

Figure 33 shows the p_T spectra of $\overline{D}^0$ and D^0 mesons separately in 0–10%, 10–20%, 20–40%, 40–60% and 60–80% centrality bins. Figure 34 shows the $\overline{D}^0/D^0$ ratio in the corresponding centrality bins. The $\overline{D}^0$ yield is significantly larger than the D^0 in the most central and mid-central collisions. Dashed lines represent constant

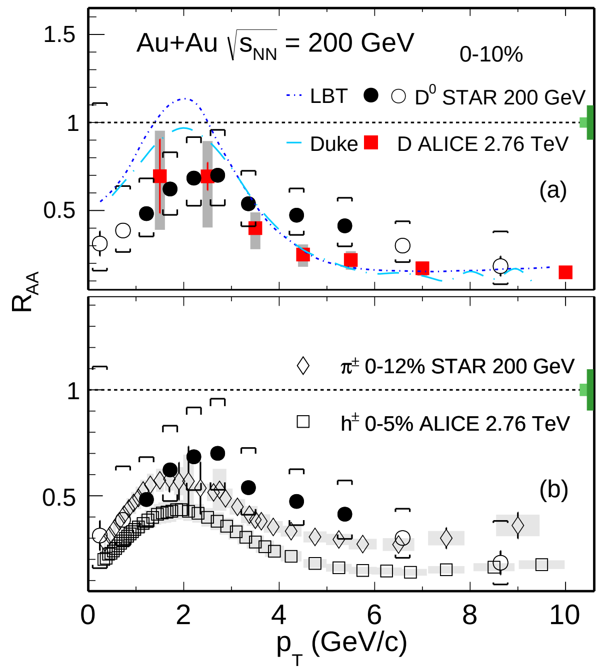

FIG. 32. D^0 $R_{\rm AA}$ in 0–10% Au+Au collisions at $\sqrt{s_{\rm NN}} = 200\,{\rm GeV}$ compared to the ALICE D-meson result in 0–10% Pb + Pb collisions at $\sqrt{s_{\rm NN}} = 2.76\,{\rm TeV}$ (a) and charged hadrons from ALICE and $\pi^{\pm}$ from STAR (b). Also shown in panel (a) are the model calculations from the LBT and Duke groups [45–47]. Notations for statistical and systematic uncertainties are the same as in previous figures.

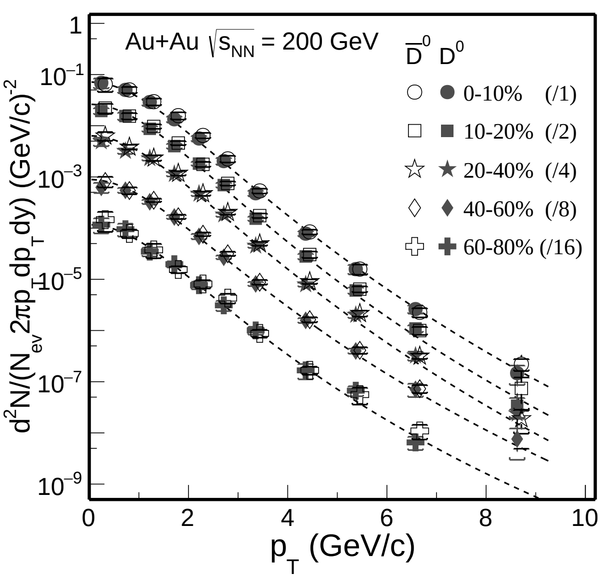

FIG. 33. D^0 and $\overline{D}^0$ invariant yields at mid-rapidity ($|y| < 1$) vs. transverse momentum for different centrality classes. Error bars (not visible for many data points) indicate statistical uncertainties and brackets depict systematic uncertainties. Global systematic uncertainties in $B.R.$ and $N_{\rm bin}$ are not plotted. Solid lines depict Levy function fits.

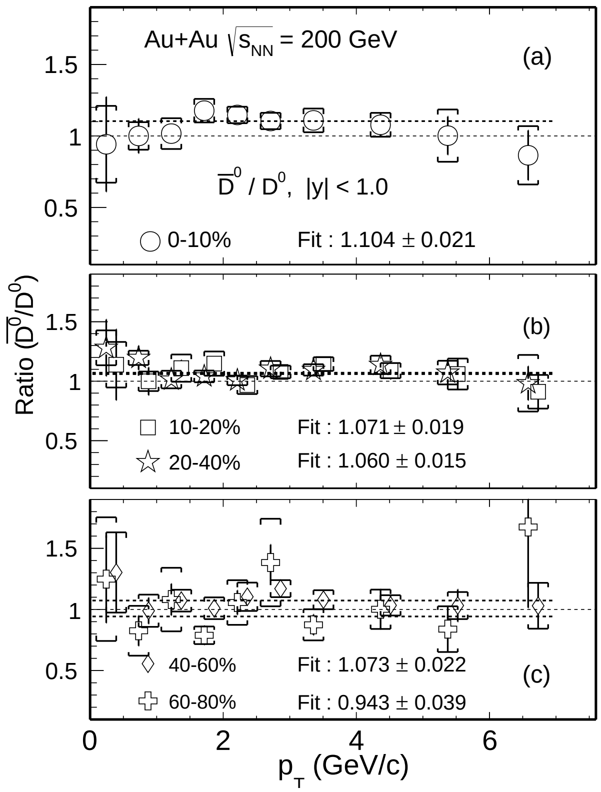

FIG. 34. $\overline{D}^0/D^0$ invariant yield ratio at mid-rapidity ($|y| < 1$) vs. transverse momentum for different centrality classes. Error bars indicate statistical uncertainties and brackets depict systematic uncertainties. Dashed lines depict constant function fits to the $\overline{D}^0/D^0$ ratios.

function fits to the $\overline{D}^0/D^0$ ratio in each centrality bin by combining the point-by-point statistical and systematic uncertainties. Table VII lists the fitted results for the $\overline{D}^0/D^0$ ratio from various centralities. In the most central collisions, $\overline{D}^0$ yield is higher than the D^0 yield by $\sim$4.9σ. The total charm quark and anti-charm quark should be conserved since they are created in pairs. A thermal model calculation predicts that the Λ_c^-/Λ_c^+ ratio will be smaller than unity at RHIC due to the finite baryon density [51]. This will then yield more $\overline{D}^0$ mesons formed than D^0 mesons in Au+Au collisions at RHIC. To verify the total charm quark conservation, one would need precise measurements of D^+/D^-, D_s^+/D_s^- as well as Λ_c^+/Λ_c^- ratios in the future.

E. Comparison to Models

Over the past several years, there have been rapid developments in the theoretical calculations on the charm hadron production [52, 53]. Here we compare our measurements to several recent calculations based on the Duke model and the Linearized Boltzmann Transport

TABLE VII. $\overline{D}^0/D^0$ ratio for various centrality bins obtained from the fit to data distributions in Fig. 34.

Centrality	$\overline{D}^0/D^0$
0–10 %	1.104 ± 0.021
10–20 %	1.071 ± 0.019
20–40 %	1.060 ± 0.015
40–60 %	1.073 ± 0.022
60–80 %	0.943 ± 0.039

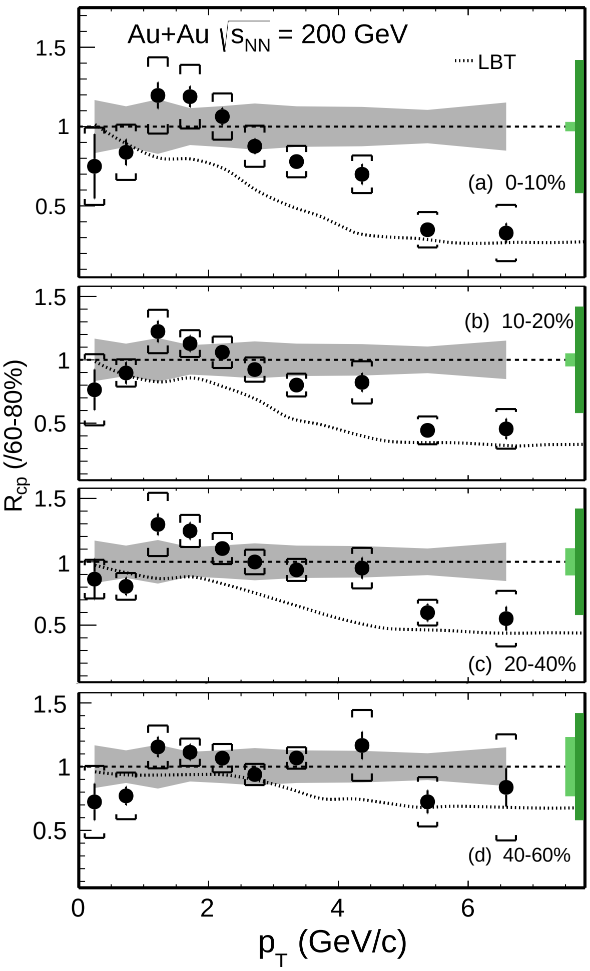

FIG. 35. D^0 R_{CP} with the 60–80% spectrum as the reference for different centrality classes compared to the LBT model calculations shown by dashed lines [45, 46]. Data points shown here are the same as in Fig. 29.

(LBT) model.

The Duke model [47, 54] uses a Langevin stochastic simulation to trace the charm quark propagation inside the QGP medium. Both collisional and radiative energy losses are included in the calculation and charm quarks are hadronized via a hybrid approach combining both coalescence and fragmentation mechanisms. The bulk medium is simulated using a viscous hydrodynamic evolution and a hadronic cascade evolution using the UrQMD model [55]. The charm quark interaction with the medium is characterized using a temperature and momentum-dependent diffusion coefficient. The medium parameters have been constrained via a statistical Bayesian analysis by fitting the previous experimental data of R_{AA} and v_2 of light, strange and charm hadrons [47]. The extracted charm quark spatial diffusion coefficient at zero momentum $2\pi T D_s|_{p=0}$ is about 1–3 near T_c and exhibits a positive slope for its temperature dependence above T_c.

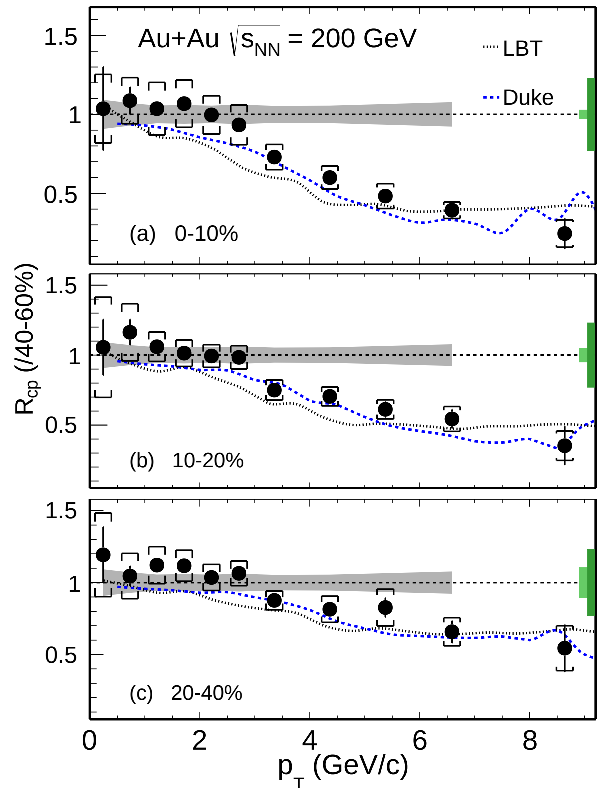

FIG. 36. D^0 R_{CP} with the 40–60% spectrum as the reference for different centrality classes compared to model calculations from LBT (black dashed lines) and Duke (blue dashed lines) groups [45–47]. Data points shown here are the same as in Fig. 30.

The Linearized Boltzmann Transport (LBT) calculation [45] extends the LBT approach developed before to include both light and heavy flavor parton evolution in the QGP medium. The transport calculation includes all $2 \rightarrow 2$ elastic scattering processes for collisional energy loss and the higher-twist formalism for medium induced radiative energy loss. It uses the same hybrid approach as in the Duke model for charm quark hadronization. The heavy quark transport is coupled with a 3D viscous hydrodynamic evolution which is tuned for light flavor hadron data. The charm quark spatial diffusion coefficient is estimated via the $2\pi T D_s = 8\pi/\hat{q}$ ($\hat{q}$, is the quark transport coefficient due to elastic scatterings) at parton momentum $p = 10\,\mathrm{GeV}/c$. The $2\pi T D_s$ is $\sim$3 at T_c and increases to $\sim$6 at $T = 500\,\mathrm{MeV}$ [46].

Figures 35 and 36 show the measured D^0 R_{CP} compared to the Duke and LBT model calculations with the 60–80% and 40–60% reference spectra respectively. The R_{CP} curves from these models are calculated based on the D^0 spectra provided by each group [45–47]. The Duke model did not calculate the spectra in the 60–80% centrality bin due to the limitation of the viscous hydrodynamic implementation. In Fig. 32 for the most central collisions, there are also calculations for the D^0 R_{AA} from the Duke and LBT group, respectively. These two models also have the predictions for the D^0 v_2 measurements for Au+Au collisions at $\sqrt{s_{\mathrm{NN}}} = 200\,\mathrm{GeV}$ [16]. Both model calculations match our new measured R_{CP} data well. The much improved precision of these new measurements are expected to further constrain the theoretical model uncertainties in these calculations.

VII. CONCLUSIONS

In summary, we report the improved measurement of D^0 production invariant yield at mid-rapidity ($|y| < 1$) in Au+Au collisions at $\sqrt{s_{\mathrm{NN}}} = 200\,\mathrm{GeV}$ with the STAR HFT detector. D^0 invariant yields are presented as a function of p_T in various centrality classes. The p_T integrated D^0 production cross section per nucleon-nucleon collisions in mid-central and central Au+Au collisions seem to be smaller than that measured in p+p collisions by 1.5σ, indicating that CNM effects and/or hadronization through quark coalescence may play an important role in Au+Au collisions. This calls for precise measurements of D^0 production in p/d+A collisions to understand the CNM effects as well as other charm hadron states in heavy-ion collisions to better constrain the total charm quark yield.

The $\overline{D}^0$ yield is observed to be higher than the D^0 in the most central collisions, by $\sim 4.9\sigma$ on average. This is potentially consistent with the picture of the finite baryon density of the system at RHIC, from which we expect the Λ_c^-/Λ_c^+ ratio to be smaller than unity and results in larger $\overline{D}^0$ yield than the D^0.

The D^0 spectra at low p_T and m_T regions are fit to the exponential function and the (Tsallis) Blast-Wave model to study the D^0 meson radial collectivity. The slope parameter extracted from the exponential function fit for D^0 mesons follows the same linearly increasing trend vs. particle mass as ϕ, Λ, Ξ^-, Ω^- particles, but different from the trend of π, K, p particles. The extracted kinetic freeze-out temperature and transverse velocity from the Blast-Wave model fit are comparable to the fit results of ϕ, Ξ^- multi-strange-quark hadrons, but different from those of π, K, p. These suggest that D^0 hadrons show a radial collective behavior with the medium, but freeze out from the system earlier and gain less radial collectivity compared to π, K, p particles. This observation is consistent with collective behavior observed in v_2 measurements. The fit results also suggest that D^0 mesons have similar kinetic freeze-out properties as multi-strange-quark hadrons ϕ, Ξ^-.

The nuclear modification factors R_{CP} of D^0 mesons are presented with both 60–80% and 40–60% centrality spectra as the reference, respectively. The D^0 R_{CP} is significantly suppressed at high p_T and the suppression level is comparable to that of light hadrons at $p_T > 5\,\mathrm{GeV/c}$, re-affirming our previous observation [12]. This indicates that charm quarks lose significant energy when traversing through the hot QCD medium. The D^0 R_{CP} is above the light hadron R_{CP} at low p_T. We compare our D^0 R_{CP} measurements to two recent theoretical model calculations from LBT and Duke group. These two models have the $2\pi T D_s$ value around 1-3 near T_c and agree with our new R_{CP} measurements. We expect the new data points with much improved precision can be used in the future to further constrain our understanding of the charm-medium interactions as well as to better determine the medium transport parameter.

VIII. ACKNOWLEDGEMENT

We thank the RHIC Operations Group and RCF at BNL, the NERSC Center at LBNL, and the Open Science Grid consortium for providing resources and support. This work is supported in part by the Office of Nuclear Physics within the U.S. DOE Office of Science, the U.S. National Science Foundation, the Ministry of Education and Science of the Russian Federation, National Natural Science Foundation of China, Chinese Academy of Science, the Ministry of Science and Technology of China and the Chinese Ministry of Education, the National Research Foundation of Korea, GA and MSMT of the Czech Republic, Department of Atomic Energy and Department of Science and Technology of the Government of India; the National Science Centre of Poland, National Research Foundation, the Ministry of Science, Education and Sports of the Republic of Croatia, RosAtom of Russia and German Bundesministerium fur Bildung, Wissenschaft, Forschung and Technologie (BMBF) and the Helmholtz Association.

[1] J. Adams *et al.* (STAR), Nucl. Phys. **A757**, 102 (2005).
[2] K. Adcox *et al.* (PHENIX), Nucl. Phys. **A757**, 184 (2005).
[3] B. Muller, J. Schukraft, and B. Wyslouch, Ann. Rev. Nucl. Part. Sci. **62**, 361 (2012).

[4] L. Adamczyk *et al.* (STAR), Phys. Rev. Lett. **116**, 062301 (2016).
[5] B. B. Abelev *et al.* (ALICE), JHEP **06**, 190 (2015).
[6] Z. Lin and M. Gyulassy, Phys. Rev. C **51**, 2177 (1995).
[7] M. Cacciari, P. Nason, and R. Vogt, Phys. Rev. Lett. **95**, 122001 (2005).
[8] G. D. Moore and D. Teaney, Phys. Rev. C **71**, 064904 (2005).
[9] B. Abelev *et al.* (ALICE), JHEP **09**, 112 (2012).
[10] J. Adam *et al.* (ALICE), JHEP **03**, 081 (2016).
[11] A. M. Sirunyan *et al.* (CMS), Physics Letters B **782**, 474 (2018).
[12] L. Adamczyk *et al.* (STAR), Phys. Rev. Lett. **113**, 142301 (2014), erratum: Phys. Rev. Lett. 121, 229901 (2018).
[13] B. Abelev *et al.* (ALICE), Phys. Rev. Lett. **111**, 102301 (2013).
[14] B. Abelev *et al.* (ALICE), Phys. Rev. C **90**, 034904 (2014).
[15] A. M. Sirunyan *et al.* (CMS), Phys. Rev. Lett. **120**, 202301 (2018).
[16] L. Adamczyk *et al.* (STAR), Phys. Rev. Lett. **118**, 212301 (2017).
[17] G. Contin *et al.*, Nucl. Instrum. Meth. **A907**, 60 (2018).
[18] M. Anderson *et al.*, Nucl. Instrum. Meth. **A499**, 659 (2003).
[19] W. J. Llope (STAR), Nucl. Instrum. Meth. **A661**, S110 (2012).
[20] L. Adamczyk *et al.* (STAR), Phys. Rev. D **86**, 072013 (2012).
[21] W. J. Llope *et al.*, Nucl. Instrum. Meth. **A522**, 252 (2004).
[22] A. Hocker *et al.*, PoS **ACAT**, 040 (2007).
[23] M. Tanabashi *et al.* (Particle Data Group), Phys. Rev. D **98**, 030001 (2018).
[24] R. Brun *et al.*, (1994), 10.17181/CERN.MUHF.DMJ1.
[25] M. Gyulassy and X.-N. Wang, Computer Physics Communications **83**, 307 (1994).
[26] J. Adams *et al.* (STAR), Phys. Rev. Lett. **92**, 112301 (2004).
[27] M. Shao *et al.*, Nucl. Instrum. Meth. **A558**, 419 (2006).
[28] Y. Xu *et al.*, Nucl. Instrum. Meth. **A614**, 28 (2010).
[29] V. Greco, C. Ko, and R. Rapp, Physics Letters B **595**, 202 (2004).
[30] Y. Oh *et al.*, Physical Review C - Nuclear Physics **79**, 1 (2009).
[31] M. He, R. J. Fries, and R. Rapp, Phys. Rev. Lett. **110**, 112301 (2013).
[32] M. Kaneta, *Thermal and Chemical Freeze-out in Heavy Ion Collisions*, Ph.D. thesis, Hiroshima U. (1999).
[33] B. I. Abelev *et al.* (STAR), Phys. Rev. Lett. **99**, 112301 (2007).
[34] J. Adams *et al.* (STAR), Phys. Rev. Lett. **98**, 062301 (2007).
[35] L. Adamczyk *et al.* (STAR), Phys. Rev. **C90**, 024906 (2014).
[36] T. Csorgo and B. Lorstad, Phys. Rev. C **54**, 1390 (1996).
[37] P. F. Kolb and U. W. Heinz, Quark Gluon Plasma 3 , 634 (2003).
[38] L. Adamczyk *et al.* (STAR), Phys. Rev. **C96**, 044904 (2017).
[39] E. Schnedermann *et al.*, Phys. Rev. **C48**, 2462 (1993).
[40] Z. Tang *et al.*, Phys. Rev. C **79**, 051901 (2009).
[41] A. Bazavov *et al.*, Phys. Rev. **D85**, 054503 (2012).
[42] B. I. Abelev *et al.* (STAR), Phys. Rev. Lett. **97**, 152301 (2006).
[43] B. I. Abelev *et al.* (STAR), Phys. Rev. C **79**, 064903 (2009).
[44] G. Agakishiev *et al.* (STAR), Phys. Rev. Lett. **108**, 072301 (2012).
[45] S. Cao *et al.*, Phys. Rev. C **94**, 014909 (2016).
[46] S. Cao, private communication.
[47] Y. Xu *et al.*, Phys. Rev. C **97**, 014907 (2018).
[48] M. Lisovyi, A. Verbytskyi, and O. Zenaiev, The European Physical Journal C **76**, 397 (2016).
[49] B. Abelev *et al.* (ALICE), Physics Letters B **720**, 52 (2013).
[50] A. Adare *et al.* (PHENIX), Phys. Rev. Lett. **101**, 232301 (2008).
[51] A. Andronic *et al.*, Physics Letters B **571**, 36 (2003).
[52] A. Beraudo *et al.*, Nucl. Phys. **A979**, 21 (2018).
[53] S. Cao *et al.*, (2018), arXiv:1809.07894 [nucl-th].
[54] S. S. Cao, G. Qin, and S. A. Bass, Phys. Rev. C **92**, 024907 (2015).
[55] M. Bleicher *et al.*, Journal of Physics G: Nuclear and Particle Physics **25**, 1859 (1999).